



1 The Eocene-Oligocene Transition in the Paratethys: Boreal Water 2 Ingression and its Paleooceanographic Implications

3 Mustafa Yücel Kaya¹, Henk Brinkhuis^{2, 3}, Chiara Fioroni⁴, Serdar Görkem Atasoy¹, Alexis Licht⁵, Dirk
4 Nürnberg⁶, Taylan Vural¹

5 ¹Department of Geological Engineering, Middle East Technical University, Ankara, 06800, Türkiye

6 ²Oceans Systems research (OCS), NIOZ Royal Netherlands Institute of Sea Research, Texel, 1790 AB The Netherlands

7 ³Earth Sciences dept., Laboratory of Palaeobotany and Palynology, Faculty of Geosciences, Utrecht University, 3584 CB
8 Utrecht, The Netherlands

9 ⁴Dipartimento di Scienze Chimiche e Geologiche, Università degli Studi di Modena e Reggio Emilia, Modena, 41121, Italy

10 ⁵Aix-Marseille Université, CNRS, IRD, INRAE, Collège de France, CEREGE, Technopôle de l'Arbois-Méditerranée, BP80,
11 13545 Aix-en-Provence, France

12 ⁶GEOMAR Helmholtz Centre for Ocean Research Kiel, Kiel, D-24148, Germany

13 *Correspondence to:* Mustafa Y. Kaya (mustafaky@gmail.com)

14 **Abstract.** The Eocene-Oligocene Transition (EOT) represents a pivotal period in Earth's climatic history, marked by the onset
15 of Antarctic glaciation and global cooling. While deep-sea records have extensively documented this transition, its impacts on
16 marginal and epicontinental seas remain less understood. This study investigates the impacts of the EOT in the Karaburun
17 composite section, located in the eastern Paratethys. Using a multidisciplinary approach that integrates biostratigraphy,
18 geochemistry, geochronology and sequence stratigraphy, a robust chronostratigraphic framework for the latest Eocene to early
19 Oligocene was established. The isotopic shifts observed in benthic and planktic foraminifera $\delta^{18}\text{O}$ and $\delta^{13}\text{C}$ records at
20 Karaburun align with global patterns but also reveal localized effects, such as freshwater influx and basin restriction, specific
21 to the semi-restricted Paratethys. The abrupt negative $\delta^{18}\text{O}$ shift across the EOB in the Paratethys reflects boreal water
22 ingressions driven by the onset of anti-estuarine circulation between the Nordic seas and Atlantic and the closure of the Arctic-
23 Atlantic gateway, which redirected cold, low-salinity boreal waters through interconnected basins towards the Paratethys.
24 These findings highlight the interplay between global climate drivers and regional hydrological dynamics, providing critical
25 insights into the evolution of marginal marine environments during the EOT. Our results underscore the significance of the
26 Paratethys as a unique archive for studying the onset of global icehouse climate conditions and regional responses.

27 1 Introduction

28 The Earth's geological history has witnessed several significant long-term climate transitions, along with short-term disruptions
29 to the carbon cycle. The most recent of these transitions occurred over the last 50 million years during the Cenozoic and is
30 characterized by a long-term cooling trend and a decline in atmospheric CO_2 levels, culminating in the onset of Antarctic
31 glaciation during the Eocene-Oligocene Transition (EOT) (e.g., Zachos et al., 2001; Caves et al., 2016). The EOT marks the
32 end of an extended period of predominantly greenhouse conditions and represents a phase of accelerated biotic change lasting



approximately 500–800 kyr, bracketing the Eocene-Oligocene Boundary (EOB) (Coxall & Pearson, 2007; Hutchinson et al., 2021). This transition is also associated with a deepening of the ocean's calcite compensation depth (CCD) (Coxall et al., 2005), a northward migration of the Intertropical Convergence Zone (ITCZ) (Hyeong et al., 2016), and increased seasonality in northern high latitudes (Eldrett et al., 2009).

The Antarctic glaciation events during the Oligocene are referred to as Oi events (Pälike et al., 2006; Pekar and Miller, 1996). At deep-ocean sites Oi glaciation events are characterized by positive excursions in the oxygen isotope records of benthic foraminifera (Miller et al., 1991; Pälike et al., 2006; Wade and Pälike, 2004). During the earliest Oligocene there are two significant cooling/glaciation events: (1) Oi-1 (Early Oligocene Glacial Maximum, EOGM of Hutchinson et al., 2020) and (2) Oi-1a, corresponding to early part of magnetic Chron C12r, took place during the early Rupelian (Pekar et al., 2002 and references therein). The EOGM, spanning 490 kyr from ~33.65 to 33.16 Ma, marks a sustained period of cold climate and glaciation during magnetic Chron C13n (Hutchinson et al., 2020). The Oi-1a glaciation event corresponds to the appearance of the cold-water dinocyst taxa *Svalbardella cooksoniae* and/or *Svalbardella* spp. in the North Sea Basin (Śliwińska, 2019a and references therein). Episodes of southward migration of *Svalbardella cooksoniae* have consequently been interpreted as evidence of cooling events (e.g., Van Simaeys et al., 2005). *Svalbardella cooksoniae* has also been documented in a brief interval during the earliest Oligocene at numerous sites across the Northern Atlantic and Western Tethyan regions (Śliwińska and Heilmann-Clausen, 2011).

The most comprehensive insights into the EOT come from deep-sea marine records of benthic foraminiferal oxygen and carbon isotopes ($\delta^{18}\text{O}$ and $\delta^{13}\text{C}$), extensively analyzed using cores from the Deep Sea Drilling Project (DSDP), Ocean Drilling Program (ODP), and Integrated Ocean Discovery Program (IODP) (e.g., Zachos et al., 1996; Pekar and Miller, 1996; Salamy and Zachos, 1999; Coxall et al., 2005; Bordiga, et al., 2015; Hutchinson et al., 2021 and references therein). In contrast, changes associated with the EOT in marginal and epicontinental seas have been the focus of relatively few studies (e.g., Pearson et al., 2008; Ozsvárt et al., 2016; van Der Boon et al., 2019; Dickson et al., 2021). Nevertheless, geochemical and sedimentary data from these shallow regions can offer valuable insights into the impacts of the EOT, including Antarctic glaciation and cooling, within restricted marine environments influenced by local factors such as freshwater influx, salinity variations, weathering, erosion and terrestrial (sediment and carbon) fluxes.

This study addresses the gap in understanding the EOT conditions in epicontinental seas by revisiting and reanalyzing an Eocene Oligocene Boundary (EOB) section in the Karaburun area of northern Türkiye (Figure 1a). The Karaburun section with its exceptionally well-preserved and diverse assemblages of microfossils (e.g. Simmons et al., 2020) provides an excellent opportunity to investigate the distribution of key latest Eocene - earliest Oligocene dinocyst and calcareous nannofossil marker species. Furthermore, it sheds light on how climatic changes influenced stratigraphic sequences in the eastern Paratethys Sea—the largest Cenozoic epicontinental sea, with no modern analogue. To investigate these processes, the EOB section at



67 Karaburun was analyzed using dinoflagellate cyst and calcareous nannofossil biostratigraphy and sequence stratigraphic
68 concepts, as well as high-resolution stable oxygen and carbon isotope analyses of benthic (*Cibicidoides* spp.) and planktic
69 (*Turborotalia ampliapertura*) foraminifera. U-Pb dating of a tuff layer within the section further constrained the age model,
70 complementing the biostratigraphic and chemostratigraphic data. The findings were compared with the EOT records from
71 other Paratethys sites and global oceans to discern the regional and global climatic and oceanographic effects.

72 2 Geological Setting

73 The interplay of paleoclimatic and tectonic processes fragmented the largely enclosed Paratethys water body into numerous
74 sub-basins, separated by narrow, shallow gateways and land bridges (Palcu et al. 2022). Extending from southern Germany to
75 China (Figure 1b), Paratethys encompassed three distinct regions. The Western and Central Paratethys are characterized by
76 active tectonics and comprised smaller, short-lived basins. The Western Paratethys included the western Alpine foreland basin,
77 while the Central Paratethys included sub-basins spanning from Austria to Romania (e.g., Popov et al., 2004). In contrast, the
78 Eastern Paratethys, centered around the Black Sea and Caspian Sea basins, evolved within a tectonically stable region (Popov
79 et al., 2004).

80

81 The Karaburun area is situated along the southern margin of the Western Black Sea Basin, a back-arc basin formed during the
82 late Cretaceous as a sub-basin of the Paratethys Sea (Okay and Nikishin, 2015) (Figure 1c). Since its formation, the Western
83 Black Sea Basin has experienced continuous subsidence, resulting in a sedimentary thickness exceeding 14 km (Okay et al.,
84 2019). To the south of the Karaburun area lies the Thrace Basin (Figure 1a), which is younger and characterized by Eocene-
85 Oligocene clastic fill deposits, reaching a maximum thickness of approximately 9 km in its central region (Turgut, 1991).
86 During the Eocene and Oligocene, the Strandja Massif—a polydeformed, deeply eroded orogenic belt composed of
87 metamorphic and magmatic rocks—formed a paleo-high that separated the Western Black Sea Basin from the Thrace Basin
88 to the south (Cattò et al., 2018) (Figure 1a). The only marine connection between these basins was through the Çatalca Gap
89 (Figure 1a), located west of İstanbul, where sedimentation abruptly ceased during the early Oligocene due to an uplift event
90 (Okay et al., 2019). This region represents the sole contact point between the Eocene-Oligocene sequences of the Black Sea
91 and Thrace Basins (Okay et al., 2019).

92 3 Regional Stratigraphy

93 The Soğucak Formation, characterized by shallow marine, massive reefal limestone, underlies the uppermost Eocene–
94 lowermost Oligocene hemipelagic deposits in both the Thrace Basin and the Karaburun area (Figure 1b). In the Karaburun
95 area, the Soğucak Formation has been dated to the Priabonian based on benthic foraminiferal biozonation (Yücel et al., 2020).
96 Overlying this formation is a 120-meter-thick sedimentary succession from the latest Eocene to early Oligocene, predominantly



composed of hemipelagic marls and carbonates (Figure 1c). This sequence also includes intermittent submarine fan deposits, debris flows, slumps, pebbly sandstones, and conglomerates near the top. A prominent tuff layer within this succession is linked to a significant Rupelian volcanic event originating from the Rhodope Massif (Marchev et al., 2024). Although the hemipelagic succession in the Karaburun area has often been referred to as the Ceylan Formation—following the terminology used in the Thrace Basin (e.g., Natal'in and Say, 2015)—we adopt the designation "İhsaniye Formation," as recommended by Okay et al. (2019) and Simmons et al. (2020). While prior studies assigned an early Oligocene age to the İhsaniye Formation in the Karaburun area (e.g., Less et al., 2011; Okay et al., 2019; Simmons et al., 2020), our findings refine its age to the latest Eocene–early Oligocene. This revision is based on the calcareous nannofossil and dinocyst biostratigraphy, stable oxygen and carbon isotope analyses, and U-Pb dating of the tuff layer.

4 Material & Methods

4.1 Lithostratigraphy

Eocene and Oligocene deposits are well-exposed in 50-meter-high cliffs along the Black Sea coast in the Karaburun area (Figure 1d). These deposits have been the focus of recent studies (e.g., Okay et al., 2019; Sancay and Bati, 2020; Simmons et al., 2020; Tulan et al., 2020), which documented their paleoenvironment, biostratigraphy, and source rock potential. To build upon these studies, we revisited the area and measured three adjacent stratigraphic sections—designated as KR1, KR2, and KR3 (Figure 1d). By integrating these sections, we constructed a composite Karaburun section comprising hemipelagic deposits of the İhsaniye Formation (Figure 2).

The studied sediments predominantly consist of hemipelagic light gray marls, dark brownish clays, thin- to medium-bedded light gray, whitish, and beige carbonates, calcareous siltstones, and sandstones, which occasionally display planar lamination. The sequence also includes submarine fan (turbiditic) conglomerates, as well as debris flow and slump deposits toward the top. The hemipelagic fine-grained deposits contain rich microfossil assemblages of planktic and benthic foraminifera, calcareous nannofossils, and dinocysts, indicating a latest Eocene–early Oligocene age (this study). The submarine fan deposits are characterized by thin to medium thick, erosive-based conglomeratic beds with mainly carbonate pebbles, organic matter, and microfossil fragments (e.g., foraminifera and shell debris) and intercalated with thin silty layers. They often grade vertically into sandstone layers. Although these submarine fan deposits exhibit variable lateral thicknesses, they provide solid key horizons for correlation of the subsections (e.g. correlation of the KR1 and KR3 subsections). Brownish organic-rich clay layers occasionally contain red-yellow nodules. Pyrite is commonly found in these organic-rich layers. Additionally, pyritized coral fossils are rarely observed in these organic-rich clay deposits. A distinctive white tuff layer at approximately 71.5 m within the composite section was sampled for U-Pb zircon dating (see section 4.5) (Figure 2). Debris flow horizons, with a maximum thickness of 5 meters, exhibit channel geometries and primarily consist of carbonate pebbles. These horizons increase in frequency toward the topmost 20 meters of the succession. This study focuses on the lower and middle portions of



the section including the EOT, ending around the tuff layer (Figure 2), and does not include analysis of the uppermost part of the succession including the debris flow deposits.

4.2 Sequence Stratigraphy

We analyzed various surfaces that indicate either a seaward or landward shift of successive facies belts, including erosive surfaces which could be equivalent to subaerial unconformities on land, transgressive surfaces, and maximum flooding surfaces. These surfaces demarcate the boundaries of different systems tracts—lowstand, transgressive, and highstand—which together form the depositional sequences (Catuneanu, 2006 and references therein).

In addition to the identification of the systems tracts based on the recognition of key surfaces, sedimentary facies and microfossil assemblages have been utilized to reconstruct past water depths and identify sea-level fluctuations, typically indicated by shifts towards offshore (or onshore) characteristics. The distribution and relative abundance of planktic and benthic foraminifera have further been employed to discern variations in relative sea level. Additionally, the relative abundance of lagoonal and inner neritic dinoflagellate cysts as well as the grain size of the deposited sediments, were examined to assess proximity to the coast.

4.3 Biostratigraphy

4.3.1 Calcareous Nannofossils

The study on Calcareous Nannofossil assemblages was carried out on 84 samples, prepared at the Department of Earth Sciences of the University of Milan (Italy), following the smear-slide standard technique described by Bown & Young (1998). Calcareous nannofossils were analyzed using an Axioscop Zeiss light microscope (LM) at 1250X magnification. Preservation of the specimens was generally good, as indicated by the presence of holococcoliths, coccospheres and small coccoliths. Quantitative analysis was performed by counting 300 specimens per sample, in a variable number of fields of view, depending on the nannofossils total abundance. Nannofossil frequency data were converted into the number of specimens per square millimeter for the evaluation of the biostratigraphic signal, and into percentages to estimate the paleoecological significance of the assemblage variations. The position of biohorizons recognized in this study is based on abundance patterns of index species, according to Agnini et al. (2014) and Viganò et al. (2023a) and are labelled as follows: Top (T): the highest occurrence of a taxon, Base common and continuous (Bc) and Top common and continuous (Tc): the lowest and highest common and continuous occurrence of a taxon. For calcareous nannofossils taxonomy, we refer to Perch-Nielsen (1985), Agnini et al. (2014), and the Nannotax web library (<https://www.mikrotax.org/Nannotax3>). The biostratigraphic schemes adopted here are those of Martini (1971) and Agnini et al. (2014).



158 4.3.2 Marine Palynology - Dinoflagellate cysts

159 For marine palynological analysis, emphasizing organic walled dinoflagellate cysts (dinocysts), 42 samples were prepared at
 160 Petrostrat laboratories (Conwy, Wales, UK; sections KR1 and KR2), and another 10 (from the sub-section KR3) at Utrecht
 161 University laboratories, according to typical palynological processing techniques (see e.g., Cramwinckel et al., 2020). This
 162 involves freeze-drying and precision weighing, subsequent HCl and HF treatments, followed by sieving residues over a 15 µm
 163 mesh sieve, before slides were produced for light microscopy from the residues. Samples are spiked with a known amount of
 164 *Lycopodium clavatum* spores to allow for absolute quantitative analysis (Stockmarr, 1972). After a broad palynofacies
 165 characterization (non-quantitative), light microscopical analysis included counting of broad categories of aquatic and terrestrial
 166 palynomorphs up to a minimum of 100 identifiable dinocysts per sample. Fragments of palynomorphs identifiable or not (viz,
 167 fragments of indeterminable palynomorphs to e.g., fragments of – therefore - indeterminable dinocysts, and including
 168 fragments of inner linings of benthic foraminifera), were quantified as well (see Table S1).

169
 170 For dinocyst taxonomy, we refer to that cited in Williams et al. (2019), except for Wetzelielloideae taxa (see discussion in Bijl
 171 et al., 2017). All materials are stored in the collection of the Marine Paleoceanography and Palynology group, at the Laboratory
 172 of Palaeobotany and Palynology (Utrecht University, Faculty of Geosciences).

173 4.4 Geochronology

174 4.4.1 U-Pb dating

175 A 30 cm-thick volcanic tuff layer was identified at the 71.5 m level of the KR composite section, serving as a key marker for
 176 constraining the age of the deposits. Three kilograms of tuff material were crushed and zircon crystals were separated by
 177 standard heavy liquid techniques and mounted in epoxy resin. Thirty five zircon crystals were dated via U-Pb at the Envitop
 178 analytical facility at CEREGE using an Element XR ICP-MS connected to a NWR193 laser (ArF 193 nm) ablation system.
 179 Zircon crystals were ablated with a 25-micron spot diameter, a 15 Hz pulse repetition rate, an energy fluence of 1.5 J/cm², and
 180 a carrier gas flow of 0.975 L/min. Data reduction, date, and date uncertainty calculations were conducted with an in-house
 181 MATLAB script. Details about our U-Pb dating workflow, data reduction steps, and discordance filter are given in Licht et al.
 182 (2024). The three zircon validation reference materials used during these sessions yielded offsets around TIMS ages < 1% in
 183 most cases, and < 2% otherwise. Out of the 35 analyzed zircon crystals, 12 yield concordant U-Pb ages (see Supplementary
 184 Table S3). The final Concordia age was calculated with concordant ages only using IsoPlotR (Vermeesch, 2018).

185 4.5 Geochemistry

186 4.5.1 δ¹⁸O & δ¹³C analyses

187 Measurements of stable oxygen (δ¹⁸O) and carbon (δ¹³C) isotopes on benthic foraminiferal (*Cibicidoides* spp.) and planktic
 188 foraminifera (*Turborotalia ampliapertura*) test fragments were performed at GEOMAR, Kiel on a Thermo Scientific MAT



253 mass spectrometer with an automated Kiel IV carbonate preparation device. The isotope values were calibrated versus the NBS 19 (National Bureau of Standards) carbonate standard and the in-house carbonate standard (“Standard Bremen”, Solnhofen limestone). Isotope values in delta-notation (δ) are reported in ‰ relative to the VPDB (Vienna Pee Dee Belemnite) scale. The long-term analytical precision is 0.06 ‰ for $\delta^{18}\text{O}$ and 0.05 ‰ for $\delta^{13}\text{C}$ (1-sigma value). Replicate measurements were not done due to the low numbers of specimens found.

5 Results

5.1 Biostratigraphy

5.1.1 Calcareous Nannofossils

So far a number of high-resolution studies on calcareous nannofossils during the EOT have been published, focusing on specific regions, including high latitudes (Villa et al., 2014) and mid- to low-latitudes (Bordiga et al., 2015; Fioroni et al., 2015; Villa et al., 2021; Jones et al., 2019). Recently, new studies on IODP sediments have further enhanced our understanding of this critical interval in the Paleogene paleoclimate history (Raffi et al., 2024, Viganò et al., 2023a, b, 2024a). Our study contributes to the knowledge of nannofossil biostratigraphy in this interval, providing detailed documentation of the EOT under marine conditions within the eastern Paratethyan realm (see Table S2 and Figure S9).

203

The extinction of *D. saipanensis* defines the base of Zone NP21 (Martini, 1971), which corresponds to the base of Zone CNE21 as described by Agnini et al. (2014). This species, as well as the “rosette shaped” *Discoaster*, is absent in the lowermost samples analyzed, indicating that its last occurrence (at 34.4 Ma) predates the studied interval.

The Base common (Bc) of *Clausicoccus subdistichus* group defines the onset of Zone CNO1 of Agnini et al. (2014), which corresponds to the upper part of Zone NP21 (Martini, 1971). The increase in abundance of this informal taxonomic group represents the most reliable nannofossil bioevent to approximate the EOB across different regions (e.g. Marino and Flores, 2002; Toffanin et al., 2013; Fioroni et al. 2015, Viganò et al., 2023a). In the studied area, this event is well-delineated, showing an abrupt increase in abundance from approximately 17 to over 100 specimens/mm² in sample N18, ca. 13 m from the base of the studied section (Figure 2).

213

The top (T) of *Ericsonia formosa* marks the base of Zone NP22 of Martini (1971) and the base of Zone CNO2 (Agnini et al., 2014). However, in the studied composite section, the precise position of this bioevent remains uncertain due to the rarity and scattered occurrence of the taxon in its final range, nevertheless it is likely located before the end of the *C. subdistichus* acme (Figure 2). This Top common (Tc) and continuous occurrence of the *C. subdistichus* group, was positioned before the top (T) of *E. formosa* by Agnini et al. (2014) in the biozonation adopted here. However, recent studies challenge this interpretation (Viganò et al., 2023a, 2024a). In fact, recent findings suggest that the top common and continuous (Tc) of this group occurs



above the top (T) of *E. formosa*, as previously reported by Backman (1987) and Catanzariti et al. (1997). The top common and continuous (Tc) of *C. subdistichus* gr., occurring early in Subchron C12r, has also been documented above the top (T) of *E. formosa* in the Pacific (Toffanin et al., 2013; Viganò et al., 2023b), the Atlantic (Bordiga et al., 2015, Viganò 2023b) and the Indian Ocean (Fioroni et al., 2015; Villa et al., 2021, Viganò 2023a). These studies indicate that *C. subdistichus* persists and remains common even after the T of *E. formosa*. In our dataset, the abundance of *C. subdistichus* exhibits a marked decrease (Tc) in the upper 5 meters of the studied section (Figure 2). Consequently, the T of *E. formosa* (i.e. the boundary between NP21 and NP22) should be positioned at some point prior to this bioevent. This interpretation is supported by data from dinoflagellates (section 5.1.2), which provide a better and more precise constraint for the stratigraphic position of the upper part of the investigated section.

5.1.2 Dinoflagellate cysts

Our work builds on the recent integrated study by Simmons et al. (2020) and notably that by Sancay and Bati (2020), targeting the Karaburun area and outcrops using palynological approaches, emphasizing dinocysts. Their pioneering effort, using more locations and sections, but with much lower sample resolution, now show the need for a higher-resolution approach, particularly while considering the potential recognition of a continuous EOT interval. Therefore, here, we focus on the lower parts of the section, with our higher-resolution sampling.

Unfortunately, palynomorph preservation and fragmentation varies significantly across the section, ranging from (most often) very poor to only occasionally reasonable, and always typically heavily fragmented (Table S1; note the high number of undeterminable - fragments of - specimens).

The dominant palynological groups throughout the succession are organic linings of benthic foraminifera, and notably their fragments, besides dinocysts, and pollen and spores of terrestrial higher plants (Table S1). We also recovered several other aquatic algal taxa and acritarchs. These include representatives of e.g., fresh to brackish water elements like *Cyclopsiella*, *Pterospermella* and, *Tasmanites* spp., besides very small ($< \sim 20 \mu\text{m}$) psilate and skolochorate cysts (viz, ‘acritarchs’, and other ‘small skolochorate cysts’) of unknown ecology. Fungal spores and fruitbodies, as well as scolecodonts are occasionally encountered as well. In terms of palynofacies (palynodebris) composition and trends, the samples are all very similar in displaying a rich mix in mainly terrestrial plant-derived elements of varying sizes, combined with various amorphous materials. Truly opaque material is conspicuously absent. No trends or breaks are apparent from this visual, non-quantitative assessment (Table S1). Overall, these results match the findings by Sancay and Bati (2020).

Although the dinocyst assemblages are difficult to quantify because of preservation and fragmentation issues, taken together, assemblages are highly diversified throughout, and essentially composed of well-known late Eocene to early Oligocene taxa (See Figure S4, S5, S6, S7 and S8). The assemblages are quite comparable to those known from other EOT sections in the



larger Tethyan region, e.g., from central and northeast Italy (Brinkhuis and Biffi, 1993; Brinkhuis, 1994; Van Mourik and Brinkhuis, 2005; Houben et al., 2012; Iakovleva, 2025), to North Africa (Egypt, El Beialy et al., 2019, Tunisia, Toricelli and Biffi, 2001, and Morocco, Chekar et al., 2018, Mahboub et al., 2019; Slimani et al., 2019; Slimani and Chekar, 2023), and further to the East, e.g., the Caspian Sea region (Bati, 2015), and Armenia (Iakovleva et al., 2024). In terms of robust dinocyst-based age-assessment, best calibrated information is available from central and northeast Italy (e.g., Brinkhuis and Biffi, 1993 and follow-up studies), including a detailed zonal scheme for the EOT matched with magneto- and calcareous microfossil stratigraphies. Based on the first, and last local occurrence of *Glaphyrocysta semitecta* the base of the Gse and the Rac/Cin zonal boundary of Brinkhuis and Biffi (1993) can be recognized in the Karaburun sections (Figure 2, Table S1). Furthermore, based on the last occurrence of *Hemiplacophora semilunifera*, the Gse/Adi zonal boundary can be recognized as well (Figure 2). Remarkably, the important index species *Areosphaeridium diktyoplokum* is so far not recorded in any of the sub-sections with confidence, hampering the recognition of the Adi/Rac zonal boundary. This is noteworthy, as elsewhere in the region, the species is typically quite abundantly present in the deposits assigned to the absolute earliest Oligocene (as defined by the extinction of the Hantkeninids, planktonic foraminifera; see e.g., Brinkhuis and Visscher, 1995; Van Mourik and Brinkhuis, 2005; Houben et al., 2012). Yet, the recognition of the other zonal boundaries allows confident correlation to the EOT interval, throughout matching the assignments by calcareous nannofossils, and the typical benthic foraminifer $\delta^{18}\text{O}$ -EOT-profile (including the Oi-1a event – cooling during the early C12r) discussed further below.

These correlations are here bolstered by the spot-occurrence of *Svalbardella cooksoniae* in sample Y41 at 71 m, assigned to the Cin Zone (Figure 2, Figure S5a, b, and c). This event was previously described from the central Italian EOT section, within the same Cin Zone (Brinkhuis and Biffi, 1993). At high northern latitudes, this species ranges from the late Eocene way into the Oligocene (e.g., Eldrett et al., 2004; Eldrett and Harding, 2009). Subsequent work noted that colder episodes during the Oligocene likely induced equatorward migration of such typical high-latitude taxa (e.g., van Simaey et al., 2005). In effect, our finding reflects the earliest one of such migration pulses, an event well documented by Śliwińska and Heilmann-Clausen (2011). These authors showed that *Svalbardella cooksoniae* is consistently present in the same narrow interval calibrated to the basal Subchron C12r, close to the NP21/NP22 boundary, in many high- and mid-latitude Northern Hemisphere sections, ranging from the Greenland Sea in the north to Italy in the south. Moreover, they correlated this event to the Oi-1a oxygen isotope maximum of Pekar and Miller (1996) and Pekar et al. (2002). Another interesting finding is specimens of the bizarre acritarch *Ascostomocystis potane* in samples from the sub-section KR2. Documented from the basal Rupelian type section in Belgium (Stover and Hardenbol, 1993), this further confirms assignment to the basal Oligocene.

5.2 U-Pb dating of the tuff

Concordia plot of the dated tuff is available in Supplementary Figure S10. The tuff sample yields an early Rupelian 32.55 ± 0.38 Ma (2σ) age, based on 11 out of the 12 dated zircons. The age of the tuff layer aligns with the biostratigraphic dating, which places the top of the KR composite section within the Cin dinoflagellate cysts zone (Figure 2).



286 5.3 Sequence Stratigraphy

287 Based on lithological, sedimentological, and paleontological characteristics, we interpret the depositional environment as a
 288 bathyal outer-shelf setting. Our sequence stratigraphic analysis identifies ten distinct depositional sequences within this setting
 289 (Figure 3). The lower part of the section, up to approximately 11 m, comprises three depositional sequences (S1, S2, and S3),
 290 characterized by intercalated pebbly/conglomeratic layers, marls, and claystones (Figure 3). The Lowstand Systems Tracts
 291 (LSTs) and Highstand Systems Tracts (HSTs) contain both pebbly/conglomeratic layers and fine-grained deposits, whereas
 292 the Transgressive Systems Tracts (TSTs) are represented exclusively by fine-grained marls and claystones. The relatively low
 293 abundance of lagoonal dinoflagellate cysts (20–40%) in this interval suggests a distal position far from the coastline. Between
 294 approximately 20 m and 23 m, within Sequence 5, the depositional setting represents the deepest marine conditions, marking
 295 a more distal position relative to the coastline. This interval corresponds to the TST within Sequence 5.

296 At around 23 m, just below the last conglomeratic layer, a maximum flooding surface marks the base of the HST within
 297 Sequence 5, coinciding with the highest percentage of lagoonal dinoflagellate cysts. This increase in lagoonal dinoflagellates
 298 (up to 60–70%) continues into the LSTs of Sequences 6 and 7, indicating a more proximal position near the coastline during
 299 the Eocene-Oligocene Glacial Maximum (EOGM).

300

301 The upper part of the section, including the Early Oligocene Cooling (see Section 6.3), consists of four sequences (S7, S8, S9,
 302 and S10). A notable difference in the thickness of the depositional sequences is observed between the lower section (up to ~11
 303 m) and the overlying sequences (from ~11 m to the top) (Figure 3). This variation in depositional thickness may be linked to
 304 orbital forcing across the late Eocene to early Oligocene (e.g., Westerhold et al., 2020).

305

306 Finally, we compared our reconstructed relative sea-level variations, based on the depositional sequences and systems tracts
 307 described above, with the global sea-level reconstruction of Miller et al. (2020) (Figure 3). In the Eastern Paratethys region,
 308 relative sea-level fluctuations during the latest Eocene and early Oligocene appear to follow a pattern parallel to global sea-
 309 level changes. (Note that the base of the Karaburun composite section is younger than 34.4 Ma, see Section 5.1.1.) These high-
 310 resolution sea-level fluctuations provide a refined reconstruction of Eastern Paratethys sea-level changes, improving upon
 311 previous studies (e.g., Popov et al., 2010).

312 5.4 Geochemistry

313 5.4.1 $\delta^{18}\text{O}$ and $\delta^{13}\text{C}$ isotope analyses

314 The $\delta^{18}\text{O}$ values of benthic foraminifera (*Cibicidoides* spp.) in the Karaburun composite section range from -9.5‰ to 1.0‰,
 315 displaying distinct temporal variations throughout the sequence. At the base of the section, at 11.40 m, just before the EOB,
 316 a small positive peak (1.0‰) is noticeable (Figure 4). Following this, a pronounced and abrupt negative shift from -0.1‰ to -
 317 9.5‰ is evident just after the Eocene-Oligocene Boundary (EOB). Following the abrupt negative shift, the $\delta^{18}\text{O}$ values increase



gradually and then sharply, reaching a peak of 1.0‰ at 19.60 m. This represents a two-phase increase in $\delta^{18}\text{O}$ during the EOT as in other EOT records (e.g., Katz et al., 2008), however, with a negative shift in between. Following the second increase, a negative shift to -2.3‰ occurs at 22 m, followed by a renewed increase in $\delta^{18}\text{O}$ values, forming a plateau that culminates at 0.6‰ by 36.75 m. The $\delta^{18}\text{O}$ values then decline, reaching a negative peak of -1.6‰ at 40.25 m, before gradually rising to 0.4‰ at 60 m, marking a second, shorter plateau. This plateau is interrupted by a decrease to -1.6‰ at 65.75 m, followed by a slight recovery to 0.5‰ at 69 m. In the uppermost portion of the section, $\delta^{18}\text{O}$ values drop to -2.4‰ at 74.50 m and then exhibit a modest increase toward the top of the section (Figure 4).

The $\delta^{13}\text{C}$ values of benthic foraminifera (*Cibicidoides* spp.) in the Karaburun composite section range from -0.7‰ to 2.2‰, exhibiting greater variability compared to the $\delta^{18}\text{O}$ values. However, similar to the $\delta^{18}\text{O}$ values, the $\delta^{13}\text{C}$ values also display a prominent shift towards more depleted levels (from 2.1‰ to 0‰) just after the EOB (Figure 5). The two-phase increase in $\delta^{13}\text{C}$ (from the EOB up to ca 24 m) is again evident, interrupted by a sharp decline (ca. 20 m) that corresponds precisely with changes in $\delta^{18}\text{O}$ (Figure 4 & 5). The $\delta^{13}\text{C}$ appears to lag behind by several tens of thousands years compared to the two-phase increase in $\delta^{18}\text{O}$ (e.g., Coxall et al., 2011). The increase just before the EOB between 11.20 m and 12 m represents a 1.3‰ shift, followed by a 1.5‰ increase between 13.20 m and 15 m and a 1.0‰ increase between 19.60 m and 23 m. Before the EOB, two more major positive carbon isotope excursions are observed at the base of the section: one between 1 and 7.5 m (1.0‰) and the second between 7.5 m and 11.20 m (0.1‰). All excursions, except the second at the base (between 7.5 m and 11.20 m), exhibit a significant positive shift of $\geq 1.0\text{‰}$. After the excursion between 19.60 m and 23 m, the $\delta^{13}\text{C}$ values drop sharply (around 23–27 m) before exhibiting another series of positive carbon isotope excursions in the middle and upper parts of the section (Figure 5). Like the excursions at the base of the section, the excursions in the middle and upper parts also display positive shifts of approximately 1‰, with the most pronounced reaching 1.5‰. This pattern reflects a dynamic carbon cycle with notable variations throughout the sequence.

Due to the intermittent presence of planktic foraminifera *Turborotalia ampliapertura* along the composite section, the $\delta^{18}\text{O}$ and $\delta^{13}\text{C}$ records of planktic foraminifera exhibit some gaps (Figures 6 and S1). Nevertheless, the overall trends and shifts remain discernible. Similar to the $\delta^{18}\text{O}$ record of benthic foraminifera, the $\delta^{18}\text{O}$ of planktic foraminifera exhibits a clear positive shift at the base of the section at 11.40 m just before the EOB, although slightly smaller (1.2‰). Following a slight positive shift (0.4‰) just after the EOB at 14.45 m, the most prominent and significant positive shift recorded by the benthic foraminifera is not fully captured in the planktic foraminifera record due to the absence of *T. ampliapertura* in the 4 m interval between 15.90 m and 19.90 m. However, the positive 2.3‰ shift observed from 15.90 to 19.90 m represents partly the major positive shift, albeit smaller than the shift recorded in the benthic foraminifera $\delta^{18}\text{O}$. An interval of ca. 7 m without any *T. ampliapertura* follows the pronounced positive shift between 19.90 m and 26.5 m, obscuring the $\delta^{18}\text{O}$ record for that interval. Following the barren interval, a gradual increase of 0.9‰ is clearly observed, extending up to 36.75 m. In the interval between



351 36.75 m and 61 m, the $\delta^{18}\text{O}$ record of planktic foraminifera fluctuates, exhibiting two significant alternating trends of decrease
 352 and increase. Following this fluctuation, a gradual decrease is observed at the top of the section, followed by a sharp decline.
 353
 354 A distinct decline in the $\delta^{13}\text{C}$ record of planktic foraminifera (1.5‰) is observed just before the EOB at 11.60 m (Figures 6
 355 and S2). Following this decline, $\delta^{13}\text{C}$ values increase at the EOB, reaching to 1.5‰ at 15.90 m with a shift of 1.8‰. Due to
 356 the infrequent presence of *T. ampliapertura*, the interval between 15.90 m and 26.5 m is not fully represented; however, this
 357 interval includes the highest $\delta^{13}\text{C}$ values observed. After these peak values, a gradual decrease is noted towards the top of the
 358 section, with six positive shifts interrupting this trend: between 34.50 m and 36.75 m, 45.20 m and 47 m, 49 m and 51 m, 56.50
 359 m and 61 m, 62.25 m and 65.75 m, and 65.75 m and 70.10 m. At the top of the section, a sharp decline in $\delta^{13}\text{C}$ values is
 360 noticeable.

361 5.5 Paleoenvironment & Paleoecology

362 5.5.1 Calcareous Nannofossils

363 Calcareous nannoplankton are highly sensitive to environmental changes in their surface water habitats, and fluctuations in
 364 nannofossil assemblages are interpreted as responses to shifts in sea surface temperature (SST), nutrient concentrations,
 365 salinity, and other environmental factors (e.g., Aubry, 1992; Winter et al., 1994) thereby reflecting palaeoceanographic
 366 perturbations. Numerous studies have explored the ecological tolerance of extinct taxa, establishing paleoecological
 367 preferences through biogeographic studies (e.g., Wei and Wise, 1990) and comparison with diverse environmental proxies
 368 (e.g., Villa et al., 2014). We discuss the behavior of several taxa within the Karaburun assemblage, based on paleoecological
 369 affinities outlined in previous works.

370
 371 *Reticulofenestra daviesii* and *Chiasmolithus* spp. are considered cool-water taxa (Wei et al., 1992; Villa et al., 2008) with
 372 preference for eutrophic conditions (Villa et al., 2014, Viganò et al., 2024b). This paleoecologic group is recorded with very
 373 low relative abundances, with few positive peaks in the middle part of the studied section. *Cyclicargolithus floridanus*, a typical
 374 eutrophic open-ocean species (Auer et al., 2014), occurs with abundances reaching up to 50% in the lower and upper part of
 375 the studied section, suggesting high productivity conditions (Aubry, 1992, Dunkley Jones et al., 2008, Villa et al., 2021) (Figure
 376 S3). Small reticulofenestrids constitute a significant component of the assemblages, reaching over 60% in the middle part of
 377 the section. They have been reported as dominant components of the nannoflora along continental margins (Haq, 1980). These
 378 settings are typically characterized by eutrophic conditions, driven by continental runoff and/or riverine input. Consequently,
 379 these small coccoliths are regarded as opportunistic taxa with broad ecological tolerance, yet particularly well-adapted to
 380 nutrient-rich environments (Aubry, 1992) and indicative of increased availability of terrigenous nutrient (Wade and Bown,
 381 2006).

382



383 The genus *Helicosphaera* has been linked to increased nutrient availability (De Kaenel and Villa, 1996; Ziveri et al., 2004).
 384 Studies on extant coccolithophorids confirm the relationship of helicosphaerids with high primary productivity rates (Haidar
 385 and Thierstein, 2001; Toledo et al., 2007), and their preference for near-shore environments (Ziveri et al., 2004; Guerreiro et
 386 al., 2005). At the Karaburun section, this genus is recorded at low abundances but occurs consistently throughout the section
 387 (Figure S3).

388
 389 Evidence of nutrient availability is further supported by the presence of braarudosphaerids, which are associated with coastal,
 390 low-salinity waters (Peleo-Alampay et al., 1999; Thierstein et al., 2004; Konno et al., 2007), eutrophic conditions (Cunha and
 391 Shimabukuro, 1997; Bartol et al., 2008) and the influx of terrigenous material (Švábenická, 1999). Braarudosphaerids are
 392 rarely found in the open ocean and thrive under unusual marine conditions, demonstrating a tolerance for environmentally
 393 stressed settings. Similar conditions are indicated by the presence of *Micrantholitus*, a taxon typically associated with shallow
 394 marine environments (Bown, 2005), reduced salinity, and eutrophic conditions (Street and Bown, 2005; Bown and Pearson
 395 2009). These penthaliths occur from the base of the investigated section, albeit at low percentages and with a discontinuous
 396 distribution, further suggesting eutrophication and reduced salinity (Figure S3).

397
 398 The presence of Ascidian spicules, with their highest and continuous occurrence in the middle-upper part of the section, also
 399 points to a shallow-marine depositional setting (e.g. Varol, 2006; Ferreira et al., 2019) and high surface-water productivity
 400 (Toledo et al., 2007). Furthermore, the relatively common occurrence of holococcoliths (mainly *Lanternithus minutus* and
 401 *Zigrablithus bijugatus*), *Pontosphaera* spp. and *Helicosphaera* spp., taxa prone to dissolution (Bown, 2005; Monechi et al.,
 402 2000) reinforces the interpretation of a shallow-water environment.

403 5.5.2 Marine Palynology - Dinoflagellate cysts

404 For the analysis of the marine palynological assemblages, emphasizing dinocysts, we rely on the taxonomical and ecological
 405 dinocyst groups derived from modern distributions (e.g., Zonneveld et al., 2013; Marret and De Vernal 2024) and empirically
 406 based paleoecological information or the Paleogene dinocysts following previous works (e.g., Brinkhuis, 1994; Pross and
 407 Brinkhuis, 2005; Sluijs et al., 2005; Frieling and Sluijs, 2018). However, as mentioned above, the assemblages are generally
 408 too poorly preserved to allow for detailed quantitative considerations. Yet, given the overall quantitative characteristics of the
 409 studied samples, viz, substantial terrestrial input, and consistent dominances of taxa empirically known from restricted marine
 410 to inner neritic (incl. lagoonal) like the goniodomid-group of dinoflagellate cysts (in this case e.g., *Homotryblium*,
 411 *Polysphaeridium*, *Heteraulacacysta*, *Eocladopyxis* spp.), and the peridinioids (*Lentinia*, *Phthanoperidinium*, *Senegalinium*,
 412 and *Deflandrea* spp.), neritic to outer neritic (e.g., *Areoligera*, *Glaphyrocysta*, *Enneadocysta*, *Spiniferites* and *Operculodinium*
 413 spp.) combined with a small, but consistent contribution from offshore, oceanic taxa like *Impagidinium* and
 414 *Nematosphaeropsis* spp. points to an essentially open marine, offshore, hemipelagic setting, comparable to e.g., the central
 415 Italian sections (cf. Brinkhuis and Biffi, 1993).



416 Despite the issues with preservation throughout, a percentage-plot of fresh water tolerant, and restricted to inner neritic marine
 417 taxa vs more offshore taxa still reveals stronger influxes in the latter part of the Gse, and within the Adi Zone (Table S1; see
 418 above, and compare e.g., Frieling and Sluijs, 2018, and Sluijs and Brinkhuis, 2024). In effect, this aspect matches the records
 419 from elsewhere (e.g., the Italian sections), and was earlier interpreted to reflect general eustatic sea level lowering associated
 420 with the Oi-1 stable isotope event reflecting the earliest glaciation of Antarctica (e.g., Brinkhuis, 1994). In terms of
 421 temperature/climatic changes, the conspicuous increase in Gymnospermous (conifer) bisaccate pollen input may be significant
 422 as well. Again, a similar trend was noted in the Italian sections across the EOT (Brinkhuis and Biffi, 1993; Brinkhuis, 1994).

423 **6 Discussion**

424 **6.1 Age control overview**

425 An initial age model for the KR composite section was constructed using tie points derived from nannofossil and dinocyst
 426 biozonations, combined with U-Pb dating of a tuff layer at 71.5 m (Figure 2). Additional age constraints were obtained by
 427 aligning the Karaburun benthic foraminifera $\delta^{18}\text{O}$ data with the high-resolution benthic foraminifera $\delta^{18}\text{O}$ record from the
 428 Atlantic sites 522 and 1263 (Figure 4). This alignment was achieved by identifying corresponding features in the isotope
 429 records, such as positive and negative shifts and their amplitudes. The carbon isotope record of benthic foraminifera provided
 430 independent validation of this tuning (Figure 5). The $\delta^{13}\text{C}$ benthic foraminifera data from the Karaburun area was correlated
 431 and aligned with global high-resolution benthic foraminifera $\delta^{13}\text{C}$ records from deep-sea sites, including 1218 (equatorial
 432 Pacific), 689 (sub-Antarctic Atlantic), 522 (South Atlantic), and 744 (southern Indian Ocean). Similarly, the planktic
 433 foraminifera provided a further confirmation for our age model (Figures S1, S2). The planktic foraminifera $\delta^{18}\text{O}$ and $\delta^{13}\text{C}$ data
 434 from the Karaburun area were correlated and aligned with high-resolution $\delta^{18}\text{O}$ and $\delta^{13}\text{C}$ records of planktic foraminifera in
 435 hemipelagic sediment cores retrieved from the African margin of the Indian Ocean (Tanzania Drilling Project sites 12 and 17,
 436 Pearson et al., 2008). All ages were assigned following the integrated magneto-biostratigraphic GTS2012 timescale. Our
 437 geochemical results indicate that the increases in $\delta^{18}\text{O}$ and $\delta^{13}\text{C}$ observed during the EOT at mid- and high-latitude sites in the
 438 South Atlantic, Southern Ocean and Pacific are also present in the Paratethys, verifying that these signals are genuinely global
 439 and valuable for stratigraphic correlation.

440 According to the constructed age model, the base of the section dates to the latest Eocene (Priabonian). The EOB is identified
 441 at 12.75 m. The middle and upper parts of the composite KR section correspond to the early Oligocene (Rupelian) (Figure 2).
 442 The revised age constraints established in this study offer a robust chronostratigraphic framework for the latest Eocene to early
 443 Oligocene interval of the Karaburun section, surpassing the accuracy of prior studies (e.g., Less et al., 2011; Okay et al., 2019;
 444 Simmons et al., 2020).



445 6.2 The EOT

446 At the deep Atlantic Site 522 and Pacific Site 1218, the Late Eocene Event is marked by a transient interval of positive $\delta^{18}\text{O}$
 447 values, reflecting a short-lived cooling or glacial episode (Hutchinson et al., 2021) (Figure 4). This isotopic shift measures
 448 approximately 0.6‰ and 0.4‰ at Site 522 and Site 1218, respectively. Similarly, the base of the KR composite section exhibits
 449 an increase of 0.7‰ in benthic foraminifera $\delta^{18}\text{O}$ values at approximately 5.5 m, which we interpret as evidence of the Late
 450 Eocene Event (Figure 4). The onset of this event coincides with the extinction of *Discoaster saipanensis* at 34.44 Ma at Site
 451 1218. Based on calcareous nannofossil data (i.e., the absence of *D. saipanensis*), the base of the KR section is inferred to be
 452 younger than 34.44 Ma, supporting this correlation. The Late Eocene Event represented by this 0.7‰ positive shift in $\delta^{18}\text{O}$
 453 values at approximately 5.5 m marks the onset of the EOT in the KR composite section (e.g., Hutchinson et al., 2020) (Figure
 454 4).

455
 456 The initial $\delta^{18}\text{O}$ step increase, occurring just before the EOB, has been identified as Step 1 in some records (e.g., EOT-1 in
 457 Katz et al., 2008; Precursor Glaciation in Scher et al., 2011). The first 1.0‰ $\delta^{18}\text{O}$ increase observed in the KR composite
 458 section at 11.40 m is interpreted as Step 1 as in the previous records (e.g., EOT-1 in Katz et al., 2008; Precursor Glaciation in
 459 Scher et al., 2011) (Figure 4). A similar $\delta^{18}\text{O}$ increase of 0.9‰ is recorded in the Alabama St. Stephens Quarry core (Miller et
 460 al., 2008). The onset of Step 1 is dated to 34.15 Ma, with an estimated duration of approximately 40 kyr (Hutchinson et al.,
 461 2020).

462
 463 The Earliest Oligocene Oxygen Isotope Step (EOIS) represents a rapid $\delta^{18}\text{O}$ increase (0.7‰ or more) occurring well after the
 464 EOB, within the lower part of Chron C13n (Hutchinson et al., 2020). The peak $\delta^{18}\text{O}$ is recorded at approximately 33.65 Ma,
 465 with the entire EOIS lasting around 40 kyr. In the KR composite section, the positive shift associated with EOIS is
 466 approximately 2‰, peaking at 1‰ at 19.60 m, marking the end of the EOT (Hutchinson et al., 2020) (Figure 4).

467
 468 The Early Oligocene Glacial Maximum (EOGM) is characterized as a prolonged period of cold climate and glaciation during
 469 the early Oligocene, corresponding to the most of magnetic Chron C13n (Hutchinson et al., 2020) (Figure 4). It spans from
 470 approximately 33.65 Ma to 33.16 Ma, lasting about 490 kyr. Correlation between the Karaburun data and global deep-sea
 471 records was achieved by aligning the peak-to-peak $\delta^{18}\text{O}$ stratigraphic intervals, starting at the top of the EOIS at 19.60 m and
 472 extending to another peak at 36.75 m (0.6‰) corresponding to the top of Chron C13n (Figure 4).

473
 474 Overall, the $\delta^{18}\text{O}$ record of benthic foraminifera from the Karaburun composite section closely mirrors global $\delta^{18}\text{O}$ trends from
 475 deep-sea sites, except for a sharp decrease observed just after the EOB (Figure 4). The EOT signal is clearly recorded in the
 476 $\delta^{18}\text{O}$ benthic foraminifera data from the Karaburun composite section. However, the relatively lower $\delta^{18}\text{O}$ values and sharp
 477 decrease just after the EOB are attributed to local conditions in the Paratethys Sea, as discussed in Section 6.4.



6.3 The Early Oligocene cooling

The presence of the cold-water dinoflagellate *Svalbardella cooksoniae* within a brief interval of the earliest Oligocene in the North Atlantic and Western Tethyan realms has been previously documented and linked to the Oi-1a oxygen isotope maximum (Śliwińska and Heilmann-Clausen, 2011). This oxygen isotope maximum representing a cooling event occurs during the early part of Chron C12r, near the NP21/NP22 boundary. In the KR composite section, the *Svalbardella cooksoniae*-bearing sample aligns with an oxygen isotope maximum at approximately 71 m, occurring during the early phase of Chron C12r (Figure 4). Consequently, the boundary between NP21 and NP22 is likely located near this level. In the North Sea, the *S. cooksoniae* event was identified at the top of the regressive systems tract (OSS-21 RST) in the 11/10-1 well (Śliwińska, 2019a). Similarly, in the KR composite section, the *S. cooksoniae* event is positioned at the top of a Lowstand Systems Tract, in agreement with the North Sea data (Figure 3). Strontium isotope analyses by Jarsve et al. (2015) suggest an age of 32.66 Ma for this event. Our U-Pb dating of the tuff layer located just above the *Svalbardella* spp.-bearing interval yields an age of 32.55 ± 0.38 Ma, aligning closely with the strontium-based age reported by Jarsve et al. (2015). These findings further support the interpretation of Śliwińska and Heilmann-Clausen (2011) that the earliest Rupelian *S. cooksoniae* interval across the Tethys, Central Europe, the North Sea Basin, the Norwegian-Greenland Sea, and the Eastern Paratethys is coeval with the Oi-1a event and corresponds to a significant sea-level fall (Figure 3).

In support of the geochemical evidence provided by $\delta^{18}\text{O}$ values in benthic foraminifera, a notable increase in gymnospermous (conifer) bisaccate pollen is clearly observed at the KR composite section during the EOT, EOGM, and Oi-1a events (Figure 3). This increase is likely associated with cooling and glaciation events occurring during these intervals, as previously suggested by Brinkhuis and Biffi (1993) and Brinkhuis (1994).

The early Oligocene cooling event (Oi-1a) was previously dated to 32.8 Ma by Pekar et al. (2002). At the KR composite section, the peak $\delta^{18}\text{O}$ values in benthic foraminifera ($\sim 0.4\text{‰}$) observed around 58–60 m are interpreted as representing the Oi-1a event. Our age model corroborates the age proposed by Pekar et al. (2002), further supporting a timing of 32.8 Ma for these peak values.

6.4 The local & global effects in the Paratethys

The benthic foraminiferal oxygen and carbon isotope records from the Karaburun area closely resemble deep-sea records from Atlantic sites 522 and 1263 during the latest Eocene and early Oligocene (Figures 4, 5). However, a notable distinction is the pronounced negative $\delta^{18}\text{O}$ shift just after the EOB, a feature characteristic of the Paratethys region (Figures 4 and 7) which will be discussed in the following. Firstly, it is noticeable that the overall benthic and planktic foraminifera $\delta^{18}\text{O}$ values are more depleted than global records from the EOT. These depleted values likely reflect a local effect rather than diagenetic alteration, as the exceptional preservation and glassy appearance of the foraminiferal shells from the KR composite section



510 and other Paratethys sites (e.g., Ozsvárt et al., 2016) suggest minimal recrystallization. A major diagenetic overprint affecting
 511 the entire basin is also improbable given the differing tectonic and depositional histories across the Paratethys sub-basins.
 512 Additionally, the observed timescale (<100 ka) and the significant magnitude of changes in proxy records from the Paratethys
 513 Basin are unlikely to be explained by regional tectonic processes. Instead, local factors such as basin restriction, enhanced
 514 precipitation and/or freshwater input due to increased runoff or changing hydrological conditions during the EOT seem more
 515 plausible explanations. Similar $\delta^{18}\text{O}$ depletion has been documented in other marginal basins during the EOT (e.g., Pearson et
 516 al., 2008; De Lira Mota et al., 2023), further supporting a localized effect in semi-restricted environments due to local
 517 hydrology. Indeed, these values are consistent with the isotopic composition of meteoric waters at mid-latitude coastal regions
 518 ($\delta^{18}\text{O} \sim -5\text{‰}$ to -10‰ ; Dansgaard, 1964; Gat, 1996). During the Rupelian (35–31 Ma), the dominant influence of Atlantic-
 519 derived westerlies likely brought increased precipitation with a depleted $\delta^{18}\text{O}$ signature to the western and central Paratethys.
 520 This interpretation was supported by $\delta^{18}\text{O}_{\text{PO}_4}$ values from herbivore tooth enamel, which reflect the depleted isotopic
 521 composition of drinking water (Kocsis et al., 2014). Modeling studies further suggest prevailing westerly winds during winter
 522 at mid-high latitudes in the Rupelian (Li et al., 2018). The "continental effect," where $\delta^{18}\text{O}$ in meteoric water becomes
 523 progressively fractionated with increasing transport distance from the Atlantic, likely contributed to more negative $\delta^{18}\text{O}$ values
 524 in the Karaburun area (e.g., Kocsis et al., 2014). Further east, evaporation over the Eastern Paratethys may have added moisture
 525 to westerly air trajectories, resulting in relatively less negative $\delta^{18}\text{O}$ values in the Northern Caucasus (Karaburun, Belaya and
 526 Chirkei sections in Figure 7) and increased inland precipitation (Figure 7). A similar precipitation gradient, with wetter
 527 conditions in the western-central Paratethys and drier conditions in the east, is also evident in an Oligocene climate
 528 reconstruction based on plant macrofossil data (Li et al., 2018). Additionally, the increased fresh water input in the Paratethys
 529 at the EOB could be plausibly explained by the major sea level fall and falling base level, driven by glacio-eustasy associated
 530 with the growth of Antarctic ice sheets during the EOT. The reorganization of rivers due to the falling base level would have
 531 introduced fresh water into the depositional epicenters of the Paratethys. Combined together, the effects of local hydrological
 532 change and the base level fall due the global major sea level fall at the EOB resulted in the depleted $\delta^{18}\text{O}$ values observed in
 533 the Paratethys. Despite the localized variations in the depletion of $\delta^{18}\text{O}$ values, the relatively consistent $\delta^{18}\text{O}$ depletion observed
 534 across Paratethys sections suggests a uniform basin-wide isotopic background. This consistency allows for reliable
 535 identification of major trends and isotopic excursions in the Paratethys Basin during the EOT.

536

537 Second to notice is that before the EOB a parallel trend could be observed for the benthic and planktic foraminifera $\delta^{18}\text{O}$ and
 538 $\delta^{13}\text{C}$ values (Figure 6). Particularly during the Step1 same trends in isotopic shifts could be clearly recognized. Most
 539 significantly, just after the EOB a distinct contrasting trend between benthic and planktic foraminifera $\delta^{18}\text{O}$ and $\delta^{13}\text{C}$ could be
 540 noticed (Figure 6). These contrasting trends between benthic and planktic foraminifera $\delta^{18}\text{O}$ and $\delta^{13}\text{C}$ just after the EOB suggest
 541 significant stratification and a reduction in vertical mixing. The pronounced negative $\delta^{18}\text{O}$ shift in benthic foraminifera likely
 542 reflects a significant influx of isotopically light cold freshwater into the bottom waters. The slight increase in planktic
 543 foraminifera $\delta^{18}\text{O}$ at the same time suggest that the surface waters might have become relatively saline due to evaporation



544 exceeding freshwater input in the surface layer, which would increase $\delta^{18}\text{O}$ values. Cold, freshwater inflow might have been
 545 funneled into deeper areas of the basin, displacing or mixing with bottom waters. This might have been happened through the
 546 submarine channels providing sediment-laden freshwater as underflows into the deep-marine turbiditic systems. However, this
 547 would have required an anti-estuarine circulation model where marine saltwater flows upstream and overrides the freshwater
 548 inflow. Indeed, an anti-estuarine circulation model for the early Oligocene Paratethys was proposed earlier (Dohmann, 1991)
 549 which was later supported by Schulz et al. (2005) showing also increasing surface salinities due to evaporation of marine water
 550 based on increasing di-/tri-MTTC ratios. An early anti-estuarine circulation model for the Paratethys aligns perfectly with our
 551 abovementioned stable isotope data. The deep fresh water input could be explained by the early evolution of the Paratethys
 552 (e.g., Schulz et al., 2005). Early evolution of the Paratethys was mainly controlled by narrowing seaways connecting it to the
 553 Tethys Ocean which led to ingressions of cold boreal water from the north (through Polish straits), initially as undercurrents
 554 (generating an anti-estuarine circulation) into the Eastern Paratethys first and then to Central and Western Paratethys (e. g.,
 555 Schulz et al., 2005; Soták, 2010). In parallel to the $\delta^{18}\text{O}$ values, a divergent trend could be observed between the benthic and
 556 planktic $\delta^{13}\text{C}$ values just after the EOB where benthic $\delta^{13}\text{C}$ declines largely whereas the planktic $\delta^{13}\text{C}$ shows an increase (Figure
 557 6). In addition to the boreal fresh-water ingression, enhanced organic matter production due to increased nutrient input and
 558 then the subsequent decomposition in the isolated, stratified Paratethys waters might have released light carbon into the bottom
 559 waters. Increased $\delta^{13}\text{C}$ in planktic foraminifera could have resulted from elevated primary productivity driven by increased
 560 nutrient input, which preferentially removes isotopically light carbon from surface waters during photosynthesis, leaving the
 561 remaining carbon pool enriched in heavier carbon.

562
 563 Initial boreal freshwater input by undercurrents then changes into ingressions of freshwater runoff as overflowing currents and
 564 diluting the former Paratethyan sea water (i.e., a change into estuarine circulation) (e.g., Schulz et al., 2005; Soták, 2010). This
 565 later ingression of overflowing freshwater runoff is likely due to an enhanced precipitation and represented as declining
 566 planktic foraminifera $\delta^{18}\text{O}$ and $\delta^{13}\text{C}$ values at ca. 15m (Figure 6). The $\delta^{18}\text{O}$ benthic foraminifera shows an increase during this
 567 time which is likely related to the cooling of the bottom waters where as $\delta^{13}\text{C}$ of benthic foraminifera shows a positive peak
 568 suggesting an enhanced organic carbon burial. The ingressions of freshwater runoff as overflowing currents likely formed a
 569 freshwater surface layer reducing ventilation of bottom waters. The formation of the freshwater surface layer and subsequent
 570 restricted mixing could have led pronounced stratification in the water column with isotopically lighter freshwater dominating
 571 the surface waters which is evidenced by more depleted $\delta^{18}\text{O}$ planktic foraminifera values (between 15 m and the top of the
 572 section) (Figure 6). The subsequent stratification in the water column would have exacerbated the buildup of oxygen-depleted
 573 conditions and the isotopically depleted carbon pool at the bottom. This would also favor sulfate reduction by microbial
 574 processes which produce further isotopically light carbon and reduce $\delta^{13}\text{C}$ values in an euxinic benthic environment.
 575 Consequently, stratification and reduced oxygenation must have enhanced the preservation of organic matter in bottom
 576 sediments.

577



578 The decrease in $\delta^{18}\text{O}$ of benthic foraminifera at ca. 22 m is likely related to the slight warming observed in the North Sea
 579 (Śliwińska et al., 2019b) in magnetic chron C13n above the EOIS (Figure 6). The increase in $\delta^{18}\text{O}$ planktic foraminifera after
 580 ca. 25 m up to the ca. 40-41 m is likely related with further cooling during the EOGM. A sharp declining trend could be noticed
 581 for benthic foraminifera $\delta^{13}\text{C}$ during the onset of this interval (at ca. 25 m) suggesting a relatively less organic carbon burial.
 582 This was due to a decrease in primary productivity at the surface represented by lowering $\delta^{13}\text{C}$ of planktic foraminifera and
 583 lowered terrestrial input.

584

585 The relative sea-level in the Paratethys starts to lower after ca. 40-41 m (Figure 3) which is followed by another fresh water
 586 input likely due to enhanced precipitation at ca. 45 m. This is evidenced by the depleted $\delta^{18}\text{O}$ planktic foraminifera values and
 587 an increase in terrestrial palynomorphs (Figures 3, 6). Once again this was followed by an increase in organic carbon burial
 588 represented by a peak in benthic $\delta^{13}\text{C}$ values at ca. 47 m.

589

590 During the Oi-1a cooling (between ca. 45 m and 75 m) a long-term declining trend in benthic $\delta^{13}\text{C}$ is distinctive and suggests
 591 a decrease in organic carbon burial (Figure 6). Decreasing relative sea-level and related increase in bottom current velocities
 592 and wave action combined with a decrease in fresh water input should have likely decreased the organic carbon burial
 593 suggested by decreasing benthic $\delta^{13}\text{C}$ at ca. 52 -53 m. Another fresh water ingression as surface runoff could be seen at ca. 56
 594 m represented by a sharp decrease in planktic $\delta^{18}\text{O}$ and $\delta^{13}\text{C}$. It appears that the global Oi-1a cooling signal dominates the
 595 upper part of the section between ca. 60 m and 75 m. At ca. 63 m a decrease in planktic $\delta^{18}\text{O}$ and $\delta^{13}\text{C}$ values corresponds to
 596 surface freshwater input accompanied by increased organic carbon burial (peak in benthic $\delta^{13}\text{C}$ values). A sharp decline in
 597 both benthic and planktic $\delta^{18}\text{O}$ and $\delta^{13}\text{C}$ values suggest a significant fresh water influx at ca. 65 m. The uppermost peak in
 598 benthic $\delta^{13}\text{C}$ values at ca. 70 m represents an enhanced organic carbon burial due to more favorable conditions for organic
 599 carbon sequestration provided by a relative sea level rise (e.g., lower bottom current velocities and lower wave action).

600

601 The divergent trend between benthic and planktic $\delta^{13}\text{C}$ values indicates a highly stratified Paratethys Sea from time to time
 602 and different surface and bottom carbon cycling processes after a change from anti-estuarine to estuarine circulation during
 603 the EOT. These changes reflect both regional hydrological and basin reconfiguration (restriction) controls and global climatic
 604 and eustatic shifts within the EOT. The global cooling during the EOT and Oi-1 must have amplified the stratification, reduced
 605 ventilation and triggered local environmental shifts in the semi-enclosed Paratethys Basin. These environmental shifts provided
 606 favorable conditions for the deposition of organic-rich fine grained sediments with high Total Organic Carbon (TOC) values.

607

608 Overall, this observed contrasting pattern between the isotopic values of benthic and planktic foraminifera highlights the
 609 complex interplay of global climate trends (Antarctic glaciation and global cooling) and regional factors (basin isolation and
 610 hydrological changes) during the EOT. Our findings align with the proposed isolation of the Paratethys, driven by the
 611 prolonged African-Arabian–Eurasian collision coupled with eustatic sea-level decline at the EOB and the cooling during the



612 EOT, led to the development of a distinct Paratethyan domain marked by mesophilic, humid climatic conditions and intensified
 613 runoff (Popov et al., 2002). Moreover, the observed relative sea-level fluctuations closely correspond with other
 614 reconstructions of relative sea-level changes from the latest Eocene to early Oligocene period (e.g., from the North Sea, Jarvse
 615 et al., 2015), further reinforcing the presence of a global climatic signal, as well.

616 **6.5 The Boreal water in the Paratethys during the Early Oligocene and its paleoceanographic significance**

617 The prominent negative shift in $\delta^{18}\text{O}$ of benthic foraminifera representing the boreal water ingress observed in the Karaburun
 618 composite section shortly after the EOB (ca. 33.7 Ma) appears to be widespread across the entire Paratethys Basin (Figure 7;
 619 Soták, 2010; Ozsvárt et al., 2016; Gavrilov et al., 2017; van der Boon et al., 2019). In the Eastern Paratethys, this shift appears
 620 to have occurred abruptly. A similar negative shift in $\delta^{18}\text{O}$ of bulk carbonates was also recorded further west in the West Alpine
 621 Foreland Basin (Chalufy section, Soutter et al., 2022), which connected the Western Paratethys to the Mediterranean Tethys
 622 Ocean (Figures 7, 8). Hence, the boreal water ingress into the Paratethys, beginning in the Eastern Paratethys and progressively
 623 reaching the Central and Western regions, is clearly represented by this negative shift across the entire Paratethys Basin just
 624 after EOB. This process was likely linked to the restriction or closure of the Arctic-Atlantic gateway and the onset of anti-
 625 estuarine circulation between the Atlantic and the Nordic Seas during the EOT. Together, the Atlantic-Arctic closure and onset
 626 of anti-estuarine circulation events could have triggered or intensified the Atlantic Meridional Overturning Circulation
 627 (AMOC) (e.g., Abelson and Erez, 2017; Coxall et al., 2018; Hutchinson et al., 2019).

628

629 Proxy records indicate that the Eocene Arctic Ocean was significantly fresher than today, with salinities ranging from 20 to 25
 630 psu and occasional drops below 10 psu (Brinkhuis et al., 2006; Kim et al., 2014; Waddell and Moore, 2008). The Arctic
 631 freshwater outflow into the North Atlantic may have inhibited deep-water formation during the Eocene (Baatsen et al., 2020;
 632 Hutchinson et al., 2018). Recent evidence suggests that the deepening of the Greenland–Scotland Ridge (GSR) around the
 633 EOT (just before the EOIS, ca. 33.7 Ma) facilitated increased exchange between the Atlantic and the Nordic Seas, enabling
 634 the formation of anti-estuarine circulation and the salinization of North Atlantic surface waters (Abelson and Erez, 2017; Stärz
 635 et al., 2017). Sea-level and paleo-shoreline reconstructions in the Nordic Seas support the hypothesis that the Arctic became
 636 isolated during the latest Eocene to early Oligocene due to the closure of the Arctic-Atlantic gateway (Hegewald and Jokat,
 637 2013; O'Regan et al., 2011; Hutchinson et al., 2019). Consequently, the gradual restriction of Arctic-Atlantic connectivity,
 638 followed by the onset of anti-estuarine circulation driven by the deepening of the GSR, may have played a critical role in
 639 developing a robust AMOC (e.g., Coxall et al., 2018; Hutchinson et al., 2019).

640

641 The closure of the Arctic gateway and the initiation of Nordic anti-estuarine circulation around the EOT likely enhanced deep-
 642 water formation, strengthening the Atlantic overturning circulation and establishing the interhemispheric northern-sourced
 643 circulation cell (e.g., Abelson and Erez, 2017; Coxall et al., 2018; Hutchinson et al., 2019). The onset of Nordic anti-estuarine
 644 circulation around the EOT might have likely influenced salinity gradients and circulation in connected basins like the North



645 Sea and Paratethys, contributing to the isolation and freshening of the latter (Figure 8). Our data indicate that the onset of anti-
 646 estuarine circulation in the Paratethys (ca. 33.7 Ma) coincided with its development between the Nordic Seas and the North
 647 Atlantic (Abelson and Erez, 2017). This suggests that at ca. 33.7 Ma the Paratethys with its anti-estuarine circulation was part
 648 of the interhemispheric northern-sourced circulation cell, contributing to global circulation (Figure 8). Shortly after, subsequent
 649 geographic restrictions and hydrological changes during the EOT changed this anti-estuarine circulation to an estuarine
 650 circulation (e.g. Schulz et al., 2005; Soták, 2010).

651

652 Further evidence supporting boreal water ingress and circulation through the Nordic Seas, North Sea and Paratethys comes
 653 from the distribution of *Svalbardella cooksoniae* in the Greenland, Norwegian, and North Seas, as well as in the Eastern
 654 Paratethys during the Oi-1a cooling event (Śliwińska and Heilmann-Clausen, 2011). This suggests a possible migration
 655 pathway for *Svalbardella* spp. The presence of *Svalbardella* in the Massicore and Monte Cagnero sections of central Italy
 656 (Brinkhuis and Biffi, 1993; van Mourik and Brinkhuis, 2005) aligns with our interpretation of boreal water circulation
 657 extending to the Mediterranean Tethys through the Paratethys (Figure 8). Sinking cold boreal freshwater likely propagated
 658 through interconnected Nordic marine basins, reaching the Paratethys and eventually the Mediterranean Tethys (Figure 8).
 659 The invasion of the Mediterranean Tethys by higher-latitude taxa around the EOB (Brinkhuis and Biffi, 1993) further supports
 660 this circulation pathway. The incursion of cold bottom waters into the Mediterranean Tethys during the EOT is corroborated
 661 by a marked transient increase in deep-water ostracod *Krithe* and a decline in deep-water ostracod diversity in the Massignano
 662 composite section (Slotnick and Schellenberg, 2013). The *Krithe* pulse and the subtle change in the deep-water ostracod fauna
 663 reflects intensified thermohaline flow of cooler deep waters, likely linked to boreal freshwater circulation through the
 664 Paratethys (e.g., Dall'Antonia et al., 2003; Slotnick and Schellenberg, 2013). Variations in seafloor ventilation and productivity
 665 due to changes in paleoceanographic conditions of the Tethys during the late Eocene - early Oligocene described in previous
 666 studies (Jovane et al., 2007 and references therein) are also likely related to the circulation of the boreal water.

667

668 The influence of boreal waters on the Mediterranean Tethys also explains the absence of well-defined positive $\delta^{18}\text{O}$ and $\delta^{13}\text{C}$
 669 shifts typically characterizing the EOT in Italian sections, including the GSSP for the EOB (e.g., Houben et al., 2012). Instead,
 670 these sections display distinct negative shifts in $\delta^{18}\text{O}$ and $\delta^{13}\text{C}$ bulk carbonate values around the EOB (e.g., Jovane et al., 2007;
 671 Brown et al., 2009; Jaramillo-Vogel et al., 2013), resembling the Paratethys records and likely reflecting deep boreal freshwater
 672 incursion through the Paratethys.

673 7 Conclusion

674 This study provides a comprehensive examination of the EOT and Early Oligocene cooling in the eastern Paratethys, with a
 675 focus on the Karaburun composite section. By integrating high-resolution biostratigraphy, geochemistry, sequence
 676 stratigraphy, and precise geochronology, we constructed a robust chronostratigraphic framework spanning the latest Eocene



to early Oligocene. Our findings reveal that the isotopic shifts in $\delta^{18}\text{O}$ and $\delta^{13}\text{C}$ at Karaburun site align closely with global records, underscoring the influence of global climatic drivers during this critical transition. However, significant local deviations, such as depleted $\delta^{18}\text{O}$ values and pronounced stratification, highlight the impact of regional hydrological changes and basin restriction of the Paratethys. These results emphasize the dual influence of global icehouse dynamics and regional hydrological processes on the eastern Paratethys during the EOT. The identification of key cooling events, such as the *Svalbardella* spp. event and its alignment with the Oi-1a glaciation, further enhances the utility of the Karaburun section for refining regional and global stratigraphic correlations. Additionally, the observed sequence stratigraphic patterns illustrate the interplay between eustatic sea-level changes and local depositional dynamics during this interval. The abrupt depleted values in $\delta^{18}\text{O}$ values in benthic foraminifera just after the EOB (ca. 33.7 Ma) in the Paratethys Basin is attributed to boreal water ingression, driven by the closure of the Arctic-Atlantic gateway and the onset of anti-estuarine circulation between the Nordic seas and Atlantic during the EOT. This event, which funneled low-salinity boreal water through the Nordic and North Seas into the Paratethys, aligns with the distribution of boreal taxa like *Svalbardella cooksoniae* and extends as far as the Mediterranean Tethys, explaining isotopic anomalies in these regions. Overall, the Karaburun section emerges as a critical archive for studying the EOT in epicontinental seas. Our findings contribute to a deeper understanding of how global climatic transitions manifest in marginal marine settings and highlight the potential for further high-resolution studies to refine our knowledge of early icehouse climate evolution in the Paratethys region and beyond.

Author contribution

MYK designed the study. MYK and SGA conducted fieldwork. TV prepared samples for geochemical analyses. DN performed geochemical analyses. AL conducted geochronological analysis. HB analyzed dinocyst stratigraphy. CF analyzed nannofossil stratigraphy. MYK wrote the paper with input from all authors. All authors analyzed and discussed the data.

Competing interests

The authors declare that they have no conflict of interest.

Acknowledgements

We thank Pierre Deschamps and Abel Guihou from the CEREGE Envitop analytical facility for their analytical and administrative support. Envitop has received funding from “Excellence Initiative” of Aix Marseille University A*MIDEX - DATCARB project, a French “Investissement d’avenir” program.



711 References

- 712 Abelson, M., & Erez, J. (2017). The onset of modern-like Atlantic meridional overturning circulation at the Eocene-Oligocene
 713 transition: Evidence, causes, and possible implications for global cooling. *Geochemistry, Geophysics, Geosystems*, 18(6),
 714 2177-2199.
- 715
- 716 Agnini, C., Fornaciari, E., Raffi, I., Catanzariti, R., Palike, H., Backman, J., Rio, D. (2014). Biozonation and biochronology
 717 of Paleogene calcareous nannofossils from low and middle latitudes. *Newsletters on Stratigraphy* 47, 131–181.
- 718
- 719 Aubry, M. P. (1992). 13. Late Paleogene Calcareous Nannoplankton Evolution: A Tale of Climatic Deterioration. In *Eocene-*
 720 *Oligocene Climatic and biotic evolution* (pp. 272-309). Princeton University Press Princeton.
- 721
- 722 Auer, G., Piller, W. E., & Harzhauser, M. (2014). High-resolution calcareous nannoplankton palaeoecology as a proxy for
 723 small-scale environmental changes in the Early Miocene. *Marine Micropaleontology*, 111, 53-65.
- 724
- 725 Baatsen, M., Von Der Heydt, A. S., Huber, M., Kliphuis, M. A., Bijl, P. K., Sluijs, A., & Dijkstra, H. A. (2020). The middle
 726 to late Eocene greenhouse climate modelled using the CESM 1.0. 5. *Climate of the Past*, 16(6), 2573-2597.
- 727
- 728 Bartol, M., Pavšič, J., Dobnikar, M., & Bernasconi, S. M. (2008). Unusual *Braarudosphaera bigelowii* and *Micrantholithus*
 729 *vesper* enrichment in the Early Miocene sediments from the Slovenian Corridor, a seaway linking the Central Paratethys and
 730 the Mediterranean. *Palaeogeography, Palaeoclimatology, Palaeoecology*, 267(1-2), 77-88.
- 731
- 732 Bati, Z. (2015). Dinoflagellate cyst biostratigraphy of the upper Eocene and lower Oligocene of the Kirmizitepe Section,
 733 Azerbaijan, South Caspian Basin. *Rev. Palaeobot. Palynol.* 217, 9–38.
- 734
- 735 Bijl, P. K., Brinkhuis, H., Egger, L. M., Eldrett, J. S., Frieling, J., Grothe, A., ... & Sluijs, A. (2017). Comment on ‘Wetzeliella
 736 and its allies—the ‘hole’ story: a taxonomic revision of the Paleogene dinoflagellate subfamily Wetzelielloideae’ by Williams et
 737 al.(2015). *Palynology*, 41(3), 423-429.
- 738
- 739 Brinkhuis, H., Biffi, U. (1993). Dinoflagellate cyst stratigraphy of the Eocene/Oligocene transition in central Italy. *Marine*
 740 *Micropaleontology* 22, 131– 183.
- 741
- 742 Brinkhuis, H. (1994). Late Eocene to early Oligocene dinoflagellate cysts from the Priabonian type-area (Northeast Italy):
 743 biostratigraphy and paleoenvironmental interpretation. *Palaeogeogr. Palaeoclimatol. Palaeoecol.* 107, 121-163.



- 744
- 745 Brinkhuis, H., Schouten, S., Collinson, M. E., Sluijs, A., Damsté, J. S. S., Dickens, G. R., ... & Expedition 302 Scientists.
 746 (2006). Episodic fresh surface waters in the Eocene Arctic Ocean. *Nature*, 441(7093), 606-609.
- 747
- 748 Bordiga, M., Henderiks, J., Tori, F., Monechi, S., Fenero, R., Legarda-Lisarri, A., & Thomas, E. (2015). Microfossil evidence
 749 for trophic changes during the Eocene–Oligocene transition in the South Atlantic (ODP Site 1263, Walvis Ridge). *Climate of*
 750 *the Past*, 11(9), 1249-1270.
- 751
- 752 Bown, P. R. & Young, J. R. (1998). Techniques. In P. R. Bown (Ed.), *Calcareous nannofossil biostratigraphy* (pp. 16–28).
 753 Cambridge, UK: Chapman & Hall.
- 754
- 755 Bown, P. R. (2005). Palaeogene calcareous nannofossils from the Kilwa and Lindi areas of coastal Tanzania (Tanzania Drilling
 756 Project Sites 1 to 10, 2003-4). *Journal of Nannoplankton Research*, 27(1), 21-95.
- 757
- 758 Bown, P. R. & Pearson, P. (2009). Calcareous plankton evolution and the Paleocene/Eocene thermal maximum event: New
 759 evidence from Tanzania. *Marine Micropaleontology*, 71(1-2), 60-70.
- 760
- 761 Brown, R. E., Koeberl, C., Montanari, A., & Bice, D. M. (2009). Evidence for a change in Milankovitch forcing caused by
 762 extraterrestrial events at Massignano, Italy, Eocene-Oligocene boundary GSSP.
- 763
- 764 Cattò, S., Cavazza, W., Zattin, M., & Okay, A. I. (2018). No significant Alpine tectonic overprint on the Cimmerian Strandja
 765 Massif (SE Bulgaria and NW Turkey). *International Geology Review*, 60(4), 513-529.
- 766
- 767 Catuneanu, O. (2006). *Principles of sequence stratigraphy*. Elsevier, Amsterdam. 375 pp.
- 768
- 769 Caves, J. K., Jost, A. B., Lau, K. V., & Maher, K. (2016). Cenozoic carbon cycle imbalances and a variable weathering
 770 feedback. *Earth and Planetary Science Letters*, 450, 152-163.
- 771
- 772 Chekar, M., Slimani, H., Jbari, H., Guédé, K. E., Mahboub, I., Asebriy, L., & Aassoumi, H. (2018). Eocene to Oligocene
 773 dinoflagellate cysts from the Tattofte section, western External Rif, northwestern Morocco: Biostratigraphy,
 774 paleoenvironments and paleoclimate. *Palaeogeography, Palaeoclimatology, Palaeoecology*, 507, 97-114.
- 775
- 776 Coxall, H. K., Wilson, P. A., Pälike, H., Lear, C. H., & Backman, J. (2005). Rapid stepwise onset of Antarctic glaciation and
 777 deeper calcite compensation in the Pacific Ocean. *Nature*, 433(7021), 53-57.



- 778
- 779 Coxall, H. K., & Pearson, P. N. (2007). The Eocene-Oligocene transition. *Deep Time Perspectives on Climate Change:*
 780 *Marrying the Signal From Computer Models and Biological Proxies*, 351-387.
- 781
- 782 Coxall, H. K., & Wilson, P. A. (2011). Early Oligocene glaciation and productivity in the eastern equatorial Pacific: Insights
 783 into global carbon cycling. *Paleoceanography*, 26(2).
- 784
- 785 Coxall, H. K., Huck, C. E., Huber, M., Lear, C. H., Legarda-Lisarri, A., O'regan, M., ... & Backman, J. (2018). Export of
 786 nutrient rich Northern Component Water preceded early Oligocene Antarctic glaciation. *Nature Geoscience*, 11(3), 190-196.
- 787
- 788 Cramwinckel, M. J., Coxall, H. K., Śliwińska, K. K., Polling, M., Harper, D. T., Bijl, P. K., ... & Sluijs, A. (2020). A warm,
 789 stratified, and restricted Labrador Sea across the Middle Eocene and its climatic optimum. *Paleoceanography and*
 790 *Paleoclimatology*, 35(10), e2020PA003932.
- 791
- 792 Cunha, A. S., & Shimabukuro, S. (1997). Braarudosphaera blooms and anomalous enrichments of Nannoconus: Evidence from
 793 the Turonian South Atlantic, Santos Basin, Brazil. *Journal of Nannoplankton Research*, 19(1), 51-55.
- 794
- 795 Dall'Antonia, B., Bossio, A., & Guernet, C. (2003). The Eocene/Oligocene boundary and the psychrospheric event in the
 796 Tethys as recorded by deep-sea ostracods from the Massignano Global Boundary Stratotype Section and Point, Central
 797 Italy. *Marine Micropaleontology*, 48(1-2), 91-106.
- 798
- 799 Dansgaard, W. (1964). Stable isotopes in precipitation. *tellus*, 16(4), 436-468.
- 800
- 801 De Kaenel, E., & Villa, G. (1996). Oligocene-Miocene calcareous nannofossil biostratigraphy and paleoecology from the
 802 Iberia Abyssal Plain. In *PROCEEDINGS-OCEAN DRILLING PROGRAM SCIENTIFIC RESULTS* (pp. 79-146). NATIONAL
 803 SCIENCE FOUNDATION.
- 804
- 805 De Lira Mota, M. A., Dunkley Jones, T., Sulaiman, N., Edgar, K. M., Yamaguchi, T., Leng, M. J., ... & Bendle, J. (2023).
 806 Multi-proxy evidence for sea level fall at the onset of the Eocene-Oligocene transition. *Nature communications*, 14(1), 4748.
- 807
- 808 Dickson, A. J., Bagard, M. L., Katchinoff, J. A., Davies, M., Poulton, S. W., & Cohen, A. S. (2021). Isotopic constraints on
 809 ocean redox at the end of the Eocene. *Earth and Planetary Science Letters*, 562, 116814.
- 810



- 811 Diester-Haass, L., & Zahn, R. (1996). Eocene-Oligocene transition in the Southern Ocean: History of water mass circulation
 812 and biological productivity. *Geology*, 24(2), 163-166.
 813
- 814 Dohmann, L. (1991). Die unteroligozänen Fische im Molassebecken. *Diss. Univ. München*.
 815
- 816 Dunkley Jones, T., Bown, P. R., Pearson, P. N., Wade, B. S., Coxall, H. K., & Lear, C. H. (2008). Major shifts in calcareous
 817 phytoplankton assemblages through the Eocene-Oligocene transition of Tanzania and their implications for low-latitude
 818 primary production. *Paleoceanography*, 23(4).
 819
- 820 El Beialy, S. Y., Head, M. J., El Atfy, H., & El Khoriby, E. M. (2019). Dinoflagellate cyst evidence for the age and
 821 palaeoenvironments of the Upper Eocene–Oligocene Dabaa Formation, Qattara Depression, north Western Desert,
 822 Egypt. *Palynology*, 43(2), 268-291.
 823
- 824 Eldrett, J. S., Harding, I. C., Firth, J. V., & Roberts, A. P. (2004). Magnetostratigraphic calibration of Eocene–Oligocene
 825 dinoflagellate cyst biostratigraphy from the Norwegian–Greenland Sea. *Marine Geology*, 204(1-2), 91-127.
 826
- 827 Eldrett, J. S., Greenwood, D. R., Harding, I. C., & Huber, M. (2009). Increased seasonality through the Eocene to Oligocene
 828 transition in northern high latitudes. *Nature*, 459(7249), 969-973.
 829
- 830 Ferreira, E. P., Alves, C. F., Sanjinés, A. E. S., & Alves, M. C. (2019). Ascidian spicules of Quaternary sediments from the
 831 lower slope of the Campos Basin (Brazil). *Quaternary International*, 508, 116-124.
 832
- 833 Fioroni, C., Villa, G., Persico, D., & Jovane, L. (2015). Middle Eocene-Lower Oligocene calcareous nannofossil
 834 biostratigraphy and paleoceanographic implications from Site 711 (equatorial Indian Ocean). *Marine Micropaleontology*, 118,
 835 50-62.
 836
- 837 Frieling, J., & Sluijs, A. (2018). Towards quantitative environmental reconstructions from ancient non-analogue microfossil
 838 assemblages: Ecological preferences of Paleocene–Eocene dinoflagellates. *Earth-Science Reviews*, 185, 956-973.
 839
- 840 Gat, J. R. (1996). Oxygen and hydrogen isotopes in the hydrologic cycle. *Annual Review of Earth and Planetary*
 841 *Sciences*, 24(1), 225-262.
 842



- 843 Gavrilov, Y. O., Shchepetova, E. V., Shcherbinina, E. A., Golovanova, O. V., Nedumov, R. I., & Pokrovsky, B. G. (2017).
 844 Sedimentary environments and geochemistry of Upper Eocene and Lower Oligocene rocks in the northeastern
 845 Caucasus. *Lithology and Mineral Resources*, 52, 447-466.
 846
- 847 Gradstein, F. M., Ogg, J. G., Schmitz, M. D., & Ogg, G. E. (2012). The geologic time scale. *Boston, USA*.
 848
- 849 Guerreiro, C., Cachão, M., & Drago, T. (2005). Calcareous nannoplankton as a tracer of the marine influence on the NW coast
 850 of Portugal over the last 14000 years. *Journal of Nannoplankton Research*, 27(2), 159-172.
 851
- 852 Haidar, A. T., & Thierstein, H. R. (2001). Coccolithophore dynamics off Bermuda (N. Atlantic). *Deep Sea Research Part II:*
 853 *Topical Studies in Oceanography*, 48(8-9), 1925-1956.
 854
- 855 Haq, B. U. (1980). Biogeographic history of Miocene calcareous nannoplankton and paleoceanography of the Atlantic
 856 Ocean. *Micropaleontology*, 414-443.
 857
- 858 Hegewald, A., & Jokat, W. (2013). Relative sea level variations in the Chukchi region-Arctic Ocean-since the late
 859 Eocene. *Geophysical Research Letters*, 40(5), 803-807.
 860
- 861 Houben, A. J., van Mourik, C. A., Montanari, A., Coccioni, R., & Brinkhuis, H. (2012). The Eocene–Oligocene transition:
 862 Changes in sea level, temperature or both?. *Palaeogeography, Palaeoclimatology, Palaeoecology*, 335, 75-83.
 863
- 864 Hutchinson, D. K., de Boer, A. M., Coxall, H. K., Caballero, R., Nilsson, J., & Baatsen, M. (2018). *Climate sensitivity and*
 865 *meridional overturning circulation in the late Eocene using GFDL CM2. 1, Clim. Past*, 14, 789–810.
 866
- 867 Hutchinson, D. K., Coxall, H. K., O'Regan, M., Nilsson, J., Caballero, R., & de Boer, A. M. (2019). Arctic closure as a trigger
 868 for Atlantic overturning at the Eocene-Oligocene Transition. *Nature Communications*, 10(1), 3797.
 869
- 870 Hutchinson, D. K., Coxall, H. K., Lunt, D. J., Steinthorsdottir, M., De Boer, A. M., Baatsen, M., ... & Zhang, Z. (2021). *The*
 871 *Eocene–Oligocene transition: a review of marine and terrestrial proxy data, models and model–data comparisons, Clim. Past*,
 872 *17*, 269–315.
 873
- 874 Hyeong, K., Kuroda, J., Seo, I., & Wilson, P. A. (2016). Response of the Pacific inter-tropical convergence zone to global
 875 cooling and initiation of Antarctic glaciation across the Eocene Oligocene Transition. *Scientific Reports*, 6(1), 30647.
 876



- 877 Iakovleva, A. I., & Heilmann-Clausen, C. (2010). Eocene dinoflagellate cyst biostratigraphy of research borehole 011-BP,
 878 Omsk region, southwestern Siberia. *Palynology*, 34(2), 195-232.
- 879
- 880 Iakovleva, A. I. (2025). Organic walled dinoflagellate cyst biostratigraphy of the Bartonian/Priabonian GSSP Alano di Piave
 881 section, NE Italy. *Review of Palaeobotany and Palynology*, 332, 105233.
- 882
- 883 Jaramillo-Vogel, D., Strasser, A., Frija, G., & Spezzaferri, S. (2013). Neritic isotope and sedimentary records of the Eocene–
 884 Oligocene greenhouse–icehouse transition: The Calcare di Nago Formation (northern Italy) in a global
 885 context. *Palaeogeography, Palaeoclimatology, Palaeoecology*, 369, 361-376.
- 886
- 887 Jarsve, E. M., Eidvin, T., Nystuen, J. P., Faleide, J. I., Gabrielsen, R. H., & Thyberg, B. I. (2015). The Oligocene succession
 888 in the eastern North Sea: basin development and depositional systems. *Geological Magazine*, 152(4), 668-693.
- 889
- 890 Jones, A. P., Dunkley Jones, T., Coxall, H., Pearson, P. N., Nala, D., & Hoggett, M. (2019). Low-latitude calcareous
 891 nannofossil response in the Indo-Pacific warm pool across the Eocene-Oligocene transition of Java,
 892 Indonesia. *Paleoceanography and Paleoclimatology*, 34(11), 1833-1847.
- 893
- 894 Jovane, L., Sprovieri, M., Florindo, F., Acton, G., Coccioni, R., Dall'Antonia, B., & Dinarès-Turell, J. (2007). Eocene–
 895 Oligocene paleoceanographic changes in the stratotype section, Massignano, Italy: Clues from rock magnetism and stable
 896 isotopes. *Journal of Geophysical Research: Solid Earth*, 112(B11).
- 897
- 898 Katz, M. E., Miller, K. G., Wright, J. D., Wade, B. S., Browning, J. V., Cramer, B. S., & Rosenthal, Y. (2008). Stepwise
 899 transition from the Eocene greenhouse to the Oligocene icehouse. *Nature geoscience*, 1(5), 329-334.
- 900
- 901 Kim, S. L., Eberle, J. J., Bell, D. M., Fox, D. A., & Padilla, A. (2014). Evidence from shark teeth for a brackish Arctic Ocean
 902 in the Eocene greenhouse. *Geology*, 42(8), 695-698.
- 903
- 904 Kocsis, L., Ozsvárt, P., Becker, D., Ziegler, R., Scherler, L., & Codrea, V. (2014). Orogeny forced terrestrial climate variation
 905 during the late Eocene–early Oligocene in Europe. *Geology*, 42(8), 727-730.
- 906
- 907 Konno, S., Harada, N., Narita, H., & Jordan, R. W. (2007). Living *Braarudosphaera bigelowii* (Gran & Braarud) Deflandre in
 908 the Bering Sea. *Journal of Nannoplankton Research*, 29(2), 78-87.
- 909



- 910 Langton, S. J., Rabideaux, N. M., Borrelli, C., & Katz, M. E. (2016). Southeastern Atlantic deep-water evolution during the
 911 late-middle Eocene to earliest Oligocene (Ocean Drilling program site 1263 and Deep Sea Drilling project site
 912 366). *Geosphere*, 12(3), 1032-1047.
- 913
- 914 Less, G., Özcan, E., & Okay, A. (2011). Stratigraphy and larger foraminifera of the Middle Eocene to Lower Oligocene
 915 shallow-marine units in the northern and eastern parts of the Thrace Basin, NW Turkey. *Turkish Journal of Earth
 916 Sciences*, 20(6), 793-845.
- 917
- 918 Li, S., Xing, Y., Valdes, P. J., Huang, Y., Su, T., Farnsworth, A., ... & Zhou, Z. (2018). Oligocene climate signals and forcings
 919 in Eurasia revealed by plant macrofossil and modelling results. *Gondwana Research*, 61, 115-127.
- 920
- 921 Licht, A., Folch, A., Sylvestre, F., Yacoub, A. N., Cogné, N., Abderamane, M., ... & Deschamps, P. (2024). Provenance of
 922 aeolian sands from the southeastern Sahara from a detrital zircon perspective. *Quaternary Science Reviews*, 328, 108539.
- 923
- 924 Mahboub, I., Slimani, H., Toufiq, A., Chekar, M., Djeya, K. L., Jbari, H., & Chakir, S. (2019). Middle Eocene to early
 925 Oligocene dinoflagellate cyst biostratigraphy and paleoenvironmental interpretations of the Ben Attaya section at Taza, eastern
 926 External Rif, Morocco. *Journal of African Earth Sciences*, 149, 154-169.
- 927
- 928 Marchev, P., Raicheva, R., Jicha, B., Guillong, M., Ivanova, R., Bachmann, O., ... & Ozsvárt, P. (2024). The large Rupelian
 929 Rhodope Massif eruptions as the source of airfall tuffs in SE, S and Central Europe: 40Ar/39Ar and U–Pb age
 930 constraints. *International Journal of Earth Sciences*, 113(7), 1619-1641.
- 931
- 932 Marino, M., & Flores, J. A. (2002). Middle Eocene to early Oligocene calcareous nannofossil stratigraphy at Leg 177 Site
 933 1090. *Marine Micropaleontology*, 45(3-4), 383-398.
- 934
- 935 Martini, E. (1971). Standard Tertiary and Quaternary calcareous nannoplankton zonation. In *Proceedings second planktonic
 936 conference, Rome* (pp. 739-785).
- 937
- 938 Miller, K. G., Wright, J. D., & Fairbanks, R. G. (1991). Unlocking the ice house: Oligocene-Miocene oxygen isotopes, eustasy,
 939 and margin erosion. *Journal of Geophysical Research: Solid Earth*, 96(B4), 6829-6848.
- 940
- 941 Miller, K. G., Browning, J. V., Aubry, M. P., Wade, B. S., Katz, M. E., Kulpecz, A. A., & Wright, J. D. (2008). Eocene–
 942 Oligocene global climate and sea-level changes: St. Stephens Quarry, Alabama. *Geological Society of America
 943 Bulletin*, 120(1-2), 34-53.



- 944
- 945 Miller, K. G., Browning, J. V., Schmelz, W. J., Kopp, R. E., Mountain, G. S., & Wright, J. D. (2020). Cenozoic sea-level and
 946 cryospheric evolution from deep-sea geochemical and continental margin records. *Science advances*, 6(20), eaaz1346.
- 947
- 948 Monechi, S., Buccianti, A., & Gardin, S. (2000). Biotic signals from nannoflora across the iridium anomaly in the upper Eocene
 949 of the Massignano section: evidence from statistical analysis. *Marine Micropaleontology*, 39(1-4), 219-237.
- 950
- 951 Natal'in, B., & Say, A. G. (2015). Eocene–Oligocene stratigraphy and structural history of the Karaburun area, southwestern
 952 Black Sea coast, Turkey: transition from extension to compression. *Geological Magazine*, 152(6), 1104-1122.
- 953
- 954 Okay, A. I., & Nikishin, A. M. (2015). Tectonic evolution of the southern margin of Laurasia in the Black Sea
 955 region. *International Geology Review*, 57(5-8), 1051-1076.
- 956
- 957 Okay, A. I., Özcan, E., Hakyemez, A., Siyako, M., Sunal, G., & Kylander-Clark, A. R. (2019). The Thrace Basin and the Black
 958 Sea: the Eocene–Oligocene marine connection. *Geological Magazine*, 156(1), 39-61.
- 959
- 960 Okay, A. I., Simmons, M. D., Özcan, E., Starkie, S., Bidgood, M. D., & Kylander-Clark, A. R. (2020). Eocene-Oligocene
 961 succession at Kızılköy (Midye) on the Black Sea coast in Thrace. *Turkish Journal of Earth Sciences*, 29(8), 139-153.
- 962
- 963 O'regan, M., Williams, C. J., Frey, K. E., & Jakobsson, M. (2011). A synthesis of the long-term paleoclimatic evolution of the
 964 Arctic. *Oceanography*, 24(3), 66-80.
- 965
- 966 Ozsvárt, P., Kocsis, L., Nyerges, A., Györi, O., & Pálffy, J. (2016). The eocene-oligocene climate transition in the central
 967 paratethys. *Palaeogeography, Palaeoclimatology, Palaeoecology*, 459, 471-487.
- 968
- 969 Palcu, D. V., & Krijgsman, W. (2023). The dire straits of Paratethys: Gateways to the anoxic giant of Eurasia. *Geological*
 970 *Society, London, Special Publications*, 523.
- 971
- 972 Pälike, H., Norris, R. D., Herrle, J. O., Wilson, P. A., Coxall, H. K., Lear, C. H., ... & Wade, B. S. (2006). The heartbeat of the
 973 Oligocene climate system. *science*, 314(5807), 1894-1898.
- 974
- 975 Pearson, P. N., McMillan, I. K., Wade, B. S., Jones, T. D., Coxall, H. K., Bown, P. R., & Lear, C. H. (2008). Extinction and
 976 environmental change across the Eocene-Oligocene boundary in Tanzania. *Geology*, 36(2), 179-182.
- 977



- 978 Pearson, P. N., Foster, G. L., & Wade, B. S. (2009). Atmospheric carbon dioxide through the Eocene–Oligocene climate
 979 transition. *Nature*, *461*(7267), 1110–1113.
 980
- 981 Pekar, S., & Miller, K. G. (1996). New Jersey Oligocene “Icehouse” sequences (ODP Leg 150X) correlated with global $\delta^{18}\text{O}$
 982 and Exxon eustatic records. *Geology*, *24*(6), 567–570.
 983
- 984 Pekar, S. F., Christie-Blick, N., Kominz, M. A., & Miller, K. G. (2002). Calibration between eustatic estimates from
 985 backstripping and oxygen isotopic records for the Oligocene. *Geology*, *30*(10), 903–906.
 986
- 987 Peleo-Alampay, A. M. (1999). Unusual Oligocene Braarudosphaera-rich layers of the South Atlantic and their
 988 palaeoceanographic implications. *J Nannoplankton Res*, *21*, 17.
 989
- 990 Perch-Nielsen, K. (1985). Cenozoic calcareous nannofossils. In H. M. Bolli, J. B. Saunders, & K. Perch-Nielsen (Eds.),
 991 *Plankton Stratigraphy* (pp. 427–554). Cambridge: Cambridge University Press.
 992
- 993 Pross, J., & Brinkhuis, H. (2005). Organic-walled dinoflagellate cysts as paleoenvironmental indicators in the Paleogene; a
 994 synopsis of concepts. *Paläontologische Zeitschrift*, *79*, 53–59.
 995
- 996 Popov, S. V., Akhmetiev, M. A., Bugrova, E. M., Lopatin, A. V., Amitrov, O. V., Andreyeva-Grigorovich, A. S., ... &
 997 Shcherba, I. G. (2002). Biogeography of the Northern Peri-Tethys from the Late Eocene to the Early Miocene: Part 2. Early
 998 Oligocene.
 999
- 1000 Popov, S. V., Rozanov, A. Y., Rögl, F., Steininger, F. F., Shcherba, I. G., & Kovac, M. (2004). Lithological-paleogeographic
 1001 maps of Paratethys. *CFS Courier Forschungsinstitut Senckenberg*, (250), 1–46.
 1002
- 1003 Popov, S. V., Antipov, M. P., Zastrozhnov, A. S., Kurina, E. E., & Pinchuk, T. N. (2010). Sea-level fluctuations on the northern
 1004 shelf of the Eastern Paratethys in the Oligocene-Neogene. *Stratigraphy and Geological Correlation*, *18*, 200–224.
 1005
- 1006 Raffi, I., Catelli, V., Fioroni, C., Righi, D., Villa, G., & Persico, D. (2024). Calcareous nannofossils from the Paleogene
 1007 Southern Ocean (IODP Site U1553, Campbell Plateau). *Newsletters on Stratigraphy*, *57*(4), 475–495.
 1008
- 1009 Sachsenhofer, R. F., Popov, S. V., Bechtel, A., Coric, S., Francu, J., Gratzner, R., ... & Vincent, S. J. (2018). Oligocene and
 1010 Lower Miocene source rocks in the Paratethys: palaeogeographical and stratigraphic controls. *Geological Society, London*,
 1011 *Special Publications*, *464*(1), 267–306.



- 1012
- 1013 Salamy, K. A., & Zachos, J. C. (1999). Latest Eocene–Early Oligocene climate change and Southern Ocean fertility: inferences
 1014 from sediment accumulation and stable isotope data. *Palaeogeography, Palaeoclimatology, Palaeoecology*, 145(1-3), 61-77.
- 1015 Sancay, R. H., & Batı, Z. (2020). Late Eocene to Early Oligocene palynostratigraphy of the Western Black Sea,
 1016 EasternParatethys. *Turkish Journal of Earth Sciences*, 29(8), 115-138.
- 1017
- 1018 Scher, H. D., Bohaty, S. M., Zachos, J. C., & Delaney, M. L. (2011). Two-stepping into the icehouse: East Antarctic weathering
 1019 during progressive ice-sheet expansion at the Eocene–Oligocene transition. *Geology*, 39(4), 383-386.
- 1020
- 1021 Schulz, H. M., Bechtel, A., & Sachsenhofer, R. F. (2005). The birth of the Paratethys during the Early Oligocene: from Tethys
 1022 to an ancient Black Sea analogue?. *Global and Planetary Change*, 49(3-4), 163-176.
- 1023
- 1024 Simmons, M. D., Bidgood, M. D., Connell, P. G., Coric, S., OKAY, A. I., Shaw, D., ... & Tari, G. C. (2020). Biostratigraphy
 1025 and paleoenvironments of the Oligocene succession (İhsaniye Formation) at Karaburun (NW Turkey). *Turkish Journal of*
 1026 *Earth Sciences*, 29(8), 28-63.
- 1027
- 1028 Slimani, H., Mahboub, I., Toufiq, A., Jbari, H., Chakir, S., & Tahiri, A. (2019). Bartonian to Priabonian dinoflagellate cyst
 1029 biostratigraphy and paleoenvironments of the M'karcha section in the Southern Tethys margin (Rif Chain, Northern
 1030 Morocco). *Marine Micropaleontology*, 153, 101785.
- 1031
- 1032 Slimani, H., & Chekar, M. (2023). Dinoflagellate-based age control and biostratigraphic correlations of the Eocene and
 1033 Oligocene (Lutetian–Chattian) sediments in the El Habt tectonic Unit, western External Rif Chain, Morocco (NW
 1034 Africa). *Newsletters on Stratigraphy*, 56(3), 257-305.
- 1035
- 1036 Śliwińska, K. K., & Heilmann-Clausen, C. (2011). *Early Oligocene cooling reflected by the dinoflagellate cyst Svalbardella*
 1037 *cooksoniae*, *Palaeogeogr. Palaeoclimatol.*, 305, 138–149.
- 1038
- 1039 Śliwińska, K. K. (2019a). Early Oligocene dinocysts as a tool for palaeoenvironment reconstruction and stratigraphical
 1040 framework—a case study from a North Sea well. *Journal of Micropalaeontology*, 38(2), 143-176.
- 1041
- 1042 Śliwińska, K. K., Thomsen, E., Schouten, S., Schoon, P. L., & Heilmann-Clausen, C. (2019b). Climate-and gateway-driven
 1043 cooling of Late Eocene to earliest Oligocene sea surface temperatures in the North Sea Basin. *Scientific Reports*, 9(1), 4458.



- 1044 Slotnick, B. S., & Schellenberg, S. A. (2013). Biotic response of Tethyan bathyal ostracodes through the Eocene–Oligocene
 1045 Transition: The composite faunal record from the Massicore and Massignano Global Stratotype Section and Point (east central
 1046 Italy). *Marine Micropaleontology*, 103, 68-84.
- 1047
- 1048 Sluijs, A., Pross, J., & Brinkhuis, H. (2005). From greenhouse to icehouse; organic-walled dinoflagellate cysts as
 1049 paleoenvironmental indicators in the Paleogene. *Earth-Science Reviews*, 68(3-4), 281-315.
- 1050
- 1051 Soták, J. (2010). Paleoenvironmental changes across the Eocene-Oligocene boundary: insights from the Central-Carpathian
 1052 Paleogene Basin. *Geologica Carpathica*, 61(5), 393.
- 1053
- 1054 Soutter, E. L., Kane, I. A., Martínez-Doñate, A., Boyce, A. J., Stacey, J., & Castelltort, S. (2022). The Eocene-Oligocene
 1055 climate transition in the Alpine foreland basin: Paleoenvironmental change recorded in submarine fans. *Palaeogeography*,
 1056 *Palaeoclimatology*, *Palaeoecology*, 600, 111064.
- 1057
- 1058 Stärz, M., Jokat, W., Knorr, G., & Lohmann, G. (2017). Threshold in North Atlantic-Arctic Ocean circulation controlled by
 1059 the subsidence of the Greenland-Scotland Ridge. *Nature communications*, 8(1), 15681.
- 1060
- 1061 Street, C., & Bown, P. R. (2000). Palaeobiogeography of early Cretaceous (Berriasian–Barremian) calcareous
 1062 nannoplankton. *Marine Micropaleontology*, 39(1-4), 265-291.
- 1063
- 1064 Stockmar, J. (1973). Determination of spore concentration with an electronic particle counter. *Danmarks Geol. Undersøgl.*,
 1065 *Række*, 15, 87-89.
- 1066
- 1067 Stover, L. E., & Hardenbol, J. (1993). Dinoflagellates and depositional sequences in the lower Oligocene (Rupelian) Boom
 1068 clay formation, Belgium. *Bulletin de la Société belge de Géologie*, 102(1-2), 5-77.
- 1069
- 1070 Švábenická, L. (1999). Braarudosphaera-rich sediments in the Turonian of the Bohemian Cretaceous Basin, Czech
 1071 Republic. *Cretaceous Research*, 20(6), 773-782.
- 1072
- 1073 Thierstein, H. R., Cortés, M. Y., & Haidar, A. T. (2004). Plankton community behavior on ecological and evolutionary time-
 1074 scales: when models confront evidence. *Coccolithophores: from molecular processes to global impact*, 455-479.
- 1075
- 1076 Toffanin, F., Agnini, C., Rio, D., Acton, G., & Westerhold, T. (2013). Middle Eocene to early Oligocene calcareous nannofossil
 1077 biostratigraphy at IODP Site U1333 (equatorial Pacific). *Micropaleontology*, 69-82.



- 1078
- 1079 Toledo, F. A., Cachão, M., Costa, K. B., & Pivel, M. A. (2007). Planktonic foraminifera, calcareous nannoplankton and
 1080 ascidian variations during the last 25 kyr in the Southwestern Atlantic: A paleoproductivity signature?. *Marine*
 1081 *Micropaleontology*, 64(1-2), 67-79.
- 1082
- 1083 Torricelli, S., & Biffi, U. (2001). Palynostratigraphy of the numidian flysch of Northern Tunisia (Oligocene-early
 1084 Miocene). *Palynology*, 25(1), 29-55.
- 1085
- 1086 Tulan, E., Sachsenhofer, R. F., Tari, G., Flecker, R., Fairbank, V., Pupp, M., & Ickert, R. B. (2020). Source rock potential and
 1087 depositional environment of the Lower Oligocene İhsaniye Formation in NW Turkey (Thrace, Karaburun). *Turkish Journal of*
 1088 *Earth Sciences*, 29(8), 64-84.
- 1089
- 1090 Turgut, S. (1991). Evolution of the Thrace sedimentary basin and its hydrocarbon prospectivity. *Generation, accumulation,*
 1091 *and production of Europe's hydrocarbons*, 415-437.
- 1092
- 1093 van Der Boon, A., van der Ploeg, R., Cramwinckel, M. J., Kuiper, K. F., Popov, S. V., Tabachnikova, I. P., ... & Krijgsman,
 1094 W. (2019). Integrated stratigraphy of the Eocene-Oligocene deposits of the northern Caucasus (Belaya River, Russia):
 1095 Intermittent oxygen-depleted episodes in the Peri-Tethys and Paratethys. *Palaeogeography, Palaeoclimatology,*
 1096 *Palaeoecology*, 536, 109395.
- 1097
- 1098 Van Mourik, C. A., & Brinkhuis, H. (2005). The Massignano Eocene-Oligocene golden spike section
 1099 revisited. *Stratigraphy*, 2(1), 13-30.
- 1100
- 1101 Van Simaey, S., Brinkhuis, H., Pross, J., Williams, G. L., & Zachos, J. C. (2005). Arctic dinoflagellate migrations mark the
 1102 strongest Oligocene glaciations. *Geology*, 33(9), 709-712.
- 1103
- 1104 Varol, O. (2006). Didemnid ascidian spicules from the Arabian Peninsula. *Journal of Nannoplankton Research*, 28(1), 35-55.
- 1105 Viganò, A., Coxall, H. K., Holmström, M., Vinco, M., Lear, C. H., & Agnini, C. (2023a). Calcareous nannofossils across the
 1106 Eocene-Oligocene transition at Site 756 (Ninetyeast Ridge, Indian Ocean): implications for biostratigraphy and
 1107 paleoceanographic clues. *Newsletters on Stratigraphy*, 56(2), 187-223.
- 1108
- 1109 Viganò, A., Westerhold, T., Bown, P. R., Jones, T. D., & Agnini, C. (2023b). Calcareous nannofossils across the Eocene-
 1110 Oligocene transition: Preservation signals and biostratigraphic remarks from ODP Site 1209 (NW Pacific, Shatsky Rise) and



- 1111 IODP Hole U1411B (NW Atlantic Ocean, Newfoundland Ridge). *Palaeogeography, Palaeoclimatology, Palaeoecology*, 629,
 1112 111778.
- 1113
- 1114 Viganò, A., Dallanave, E., Alegret, L., Westerhold, T., Sutherland, R., Dickens, G. R., ... & Agnini, C. (2024b). Calcareous
 1115 nannofossils and paleoclimatic evolution across the Eocene-Oligocene transition at IODP Site U1509, Tasman Sea, Southwest
 1116 Pacific Ocean. *Paleoceanography and Paleoclimatology*, 39(2), e2023PA004738.
- 1117
- 1118 Viganò, A., Dallanave, E., Alegret, L., Westerhold, T., Sutherland, R., Dickens, G. R., ... & Agnini, C. (2024a). Calcareous
 1119 nannofossil biostratigraphy and biochronology across the Eocene-Oligocene transition: the record at IODP Site U1509
 1120 (Tasman Sea) and a global overview. *Newsletters on Stratigraphy*, 57(1), 1-23.
- 1121
- 1122 Villa, G., Fioroni, C., Pea, L., Bohaty, S., & Persico, D. (2008). Middle Eocene–late Oligocene climate variability: calcareous
 1123 nannofossil response at Kerguelen Plateau, Site 748. *Marine Micropaleontology*, 69(2), 173-192.
- 1124
- 1125 Villa, G., Fioroni, C., Persico, D., Roberts, A. P., & Florindo, F. (2014). Middle Eocene to late Oligocene Antarctic
 1126 glaciation/deglaciation and Southern Ocean productivity. *Paleoceanography*, 29(3), 223-237.
- 1127
- 1128 Villa, G., Florindo, F., Persico, D., Lurcock, P., de Martini, A. P., Jovane, L., & Fioroni, C. (2021). Integrated calcareous
 1129 nannofossil and magnetostratigraphic record of ODP Site 709: Middle Eocene to late Oligocene paleoclimate and
 1130 paleoceanography of the Equatorial Indian Ocean. *Marine Micropaleontology*, 169, 102051.
- 1131
- 1132 Waddell, L. M., & Moore, T. C. (2008). Salinity of the Eocene Arctic Ocean from oxygen isotope analysis of fish bone
 1133 carbonate. *Paleoceanography*, 23(1).
- 1134
- 1135 Wade, B. S., & Pälike, H. (2004). Oligocene climate dynamics. *Paleoceanography*, 19(4).
- 1136
- 1137 Wade, B. S., & Bown, P. R. (2006). Calcareous nannofossils in extreme environments: the Messinian salinity crisis, Polesi
 1138 Basin, Cyprus. *Palaeogeography, Palaeoclimatology, Palaeoecology*, 233(3-4), 271-286.
- 1139
- 1140 Wei, W., & Wise Jr, S. W. (1990). Biogeographic gradients of middle Eocene-Oligocene calcareous nannoplankton in the
 1141 South Atlantic Ocean. *Palaeogeography, Palaeoclimatology, Palaeoecology*, 79(1-2), 29-61.
- 1142
- 1143 Wei, W., G. Villa, and S. W. Wise Jr. (1992). Paleoceanographic implications of Eocene-Oligocene calcareous nannofossils
 1144 from sites 711 and 748 in the Indian Ocean, *Proc. Ocean Drill. Progr. Sci. Res.*, 120, 979–999.



- 1145
- 1146 Westerhold, T., Marwan, N., Drury, A. J., Liebrand, D., Agnini, C., Anagnostou, E., ... & Zachos, J. C. (2020). An
 1147 astronomically dated record of Earth's climate and its predictability over the last 66 million years. *Science*, 369(6509), 1383-
 1148 1387.
- 1149
- 1150 Williams, G. L., Fensome, R. A., & MacRae, R. A. (2019). The Lentin and Williams Index of Fossil Dinoflagellate 2019
 1151 Edition. *AASP Contributions Series Number*, 50:1173.
- 1152
- 1153 Winter, A., and W. G. Siesser (Eds)1994. *Coccolithophores*, pp. 242, Cambridge Univ. Press, Cambridge.
- 1154
- 1155 Yücel, A. O., Özcan, E., & Erbil, Ü. (2020). Latest Priabonian larger benthic foraminiferal assemblages at the demise of
 1156 theSoğucak Carbonate Platform (Thrace Basin and Black Sea shelf, NW Turkey): implications for the shallow marine
 1157 biostratigraphy. *Turkish Journal of Earth Sciences*, 29(8), 85-114.
- 1158
- 1159 Zachos, J. C., Quinn, T. M., & Salamy, K. A. (1996). High-resolution (104 years) deep-sea foraminiferal stable isotope records
 1160 of the Eocene-Oligocene climate transition. *Paleoceanography*, 11(3), 251-266.
- 1161
- 1162 Zachos, J., Pagani, M., Sloan, L., Thomas, E., & Billups, K. (2001). Trends, rhythms, and aberrations in global climate 65 Ma
 1163 to present. *Science*, 292(5517), 686-693.
- 1164
- 1165 Ziveri, P., Baumann, K. H., Böckel, B., Bollmann, J., & Young, J. R. (2004). Biogeography of selected Holocene coccoliths
 1166 in the Atlantic Ocean. *Coccolithophores: From Molecular processes to global impact*, 403-428.
- 1167
- 1168
- 1169
- 1170
- 1171
- 1172
- 1173
- 1174
- 1175
- 1176
- 1177
- 1178

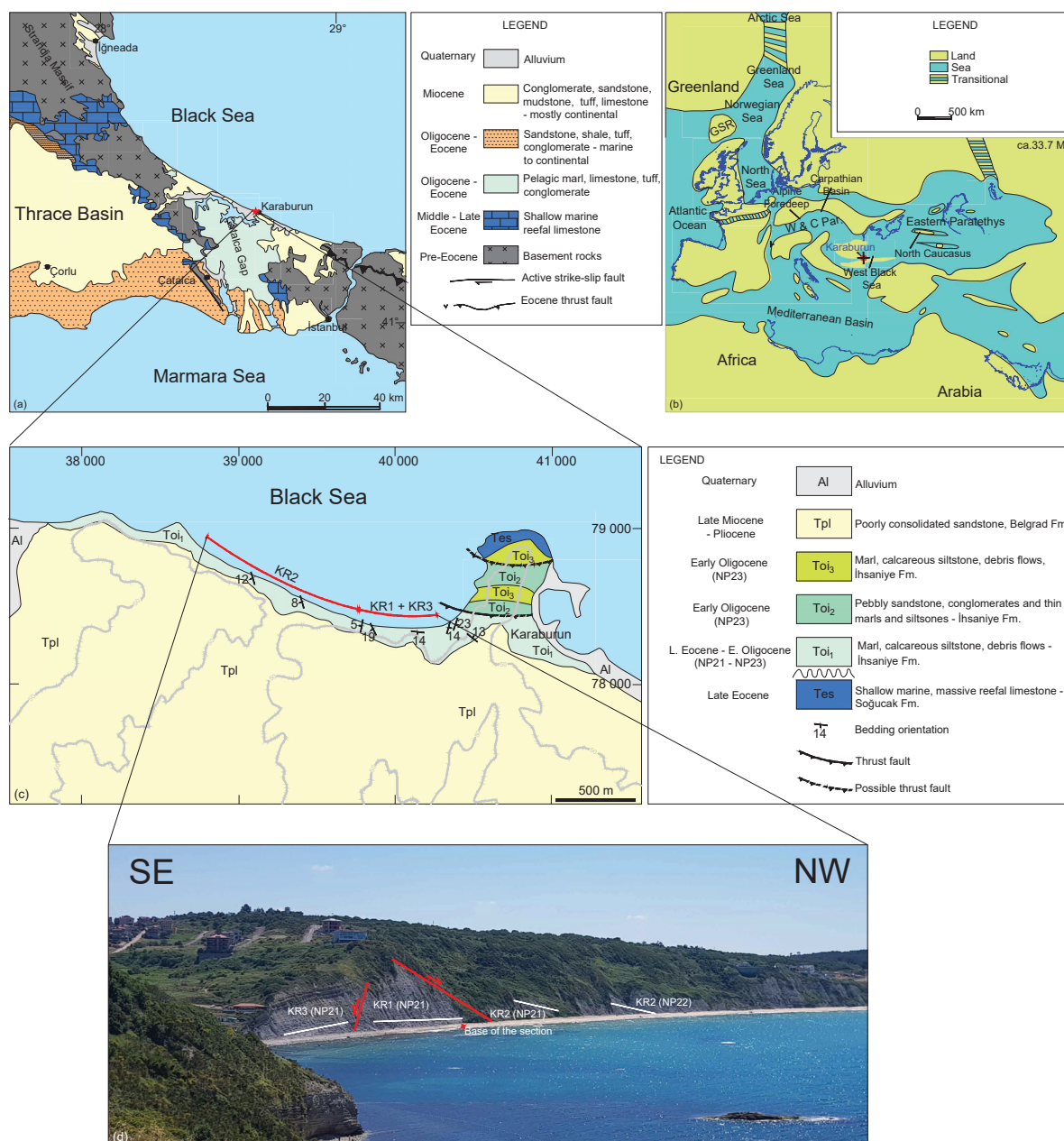


Figure 1 a) Geological map of the Thrace region (Türkiye) showing the location of the Karaburun area in relation to Thrace Basin, Strandja Massif and Çatalca Gap (modified from Okay et al., 2020). b) Paleogeography of the Paratethys during the early Oligocene (Rupelian, 33.7 Ma) (modified from Sachsenhofer et al., 2018) GSR: Greenland Scotland Ridge. W & C Par.: Western & Central Paratethys. Red dot marks the Karaburun area. c) Geological map of the Karaburun area showing the locations of the sub-sections KR1, KR2 and KR3 (revised from Okay et al., 2019). d) View of the studied sub-sections facing south from Cape Karaburun.

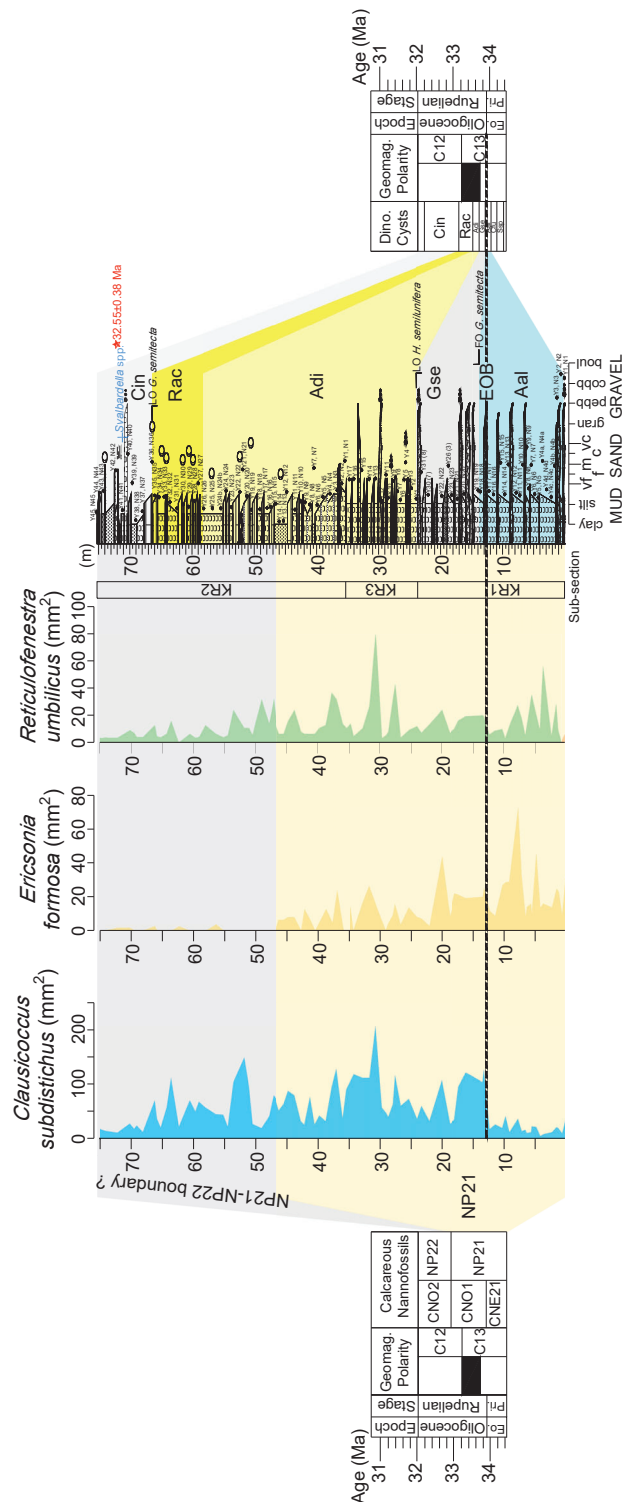


Figure 2 Stratigraphic log (in meters) of the Karaburun composite section with relative abundances of marker calcareous nannofossils. KR1, KR2, and KR3 are the abbreviations for the studied sub-sections from the Karaburun area. The biostratigraphic (calcareous nannofossil and dinoflagellate cyst) correlations to the geological time scale (Gradstein et al., 2012) are indicated by colored shading. The red star on the log shows the level of the tuff layer (32.65±0.38 Ma) while the blue cross indicates the level of sample with cold-water dinoflagellate *Svalbardella cooksoniae*, indicating a cooling event occurred during the early part of Chron C12r, near the NP21/NP22 boundary.

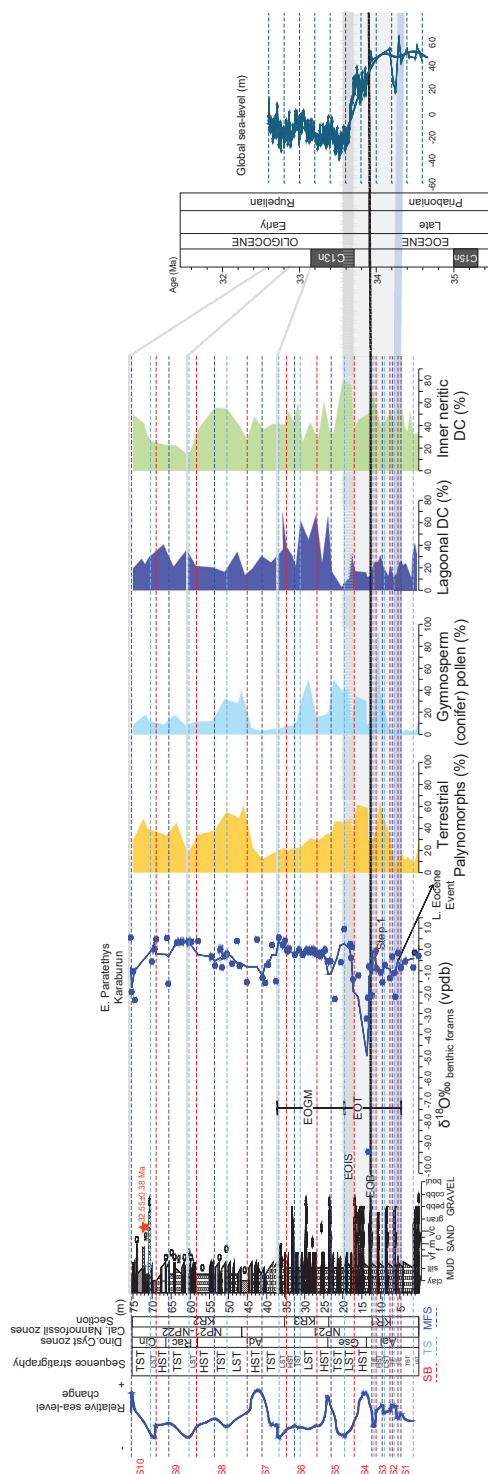


Figure 3 Stratigraphic log (in meters) of the Karaburun composite section showing sequence stratigraphic interpretations and reconstructed relative sea-level. The sequence stratigraphic interpretation and the reconstructed relative sea-level changes are based on the analysis of benthic foraminifera $\delta^{18}\text{O}$ values, along with the abundance of terrestrial palynomorphs and lagoonal and inner neritic dinocysts. Red star shows the level of the tuff layer on the log while blue cross indicates the level of sample with cold-water dinocyst *Svalbardella cooksoniae*. Correlation to the reconstructed global sea-level curve (Miller et al., 2020) and to the geological time scale (Gradstein et al., 2012) could be seen on the right side. S: Sequence, SB: Sequence boundary, TS: Transgressive surface, MFS: Maximum flooding surface, LST: Lowstand systems tract, TST: Transgressive Systems Tract. HTS: Highstand Systems Tract, EOB: Eocene Oligocene Boundary, EOT: Eocene Oligocene Transition, EOIS: Earliest Oligocene oxygen isotope step, EOGM: Early Oligocene glacial maximum.

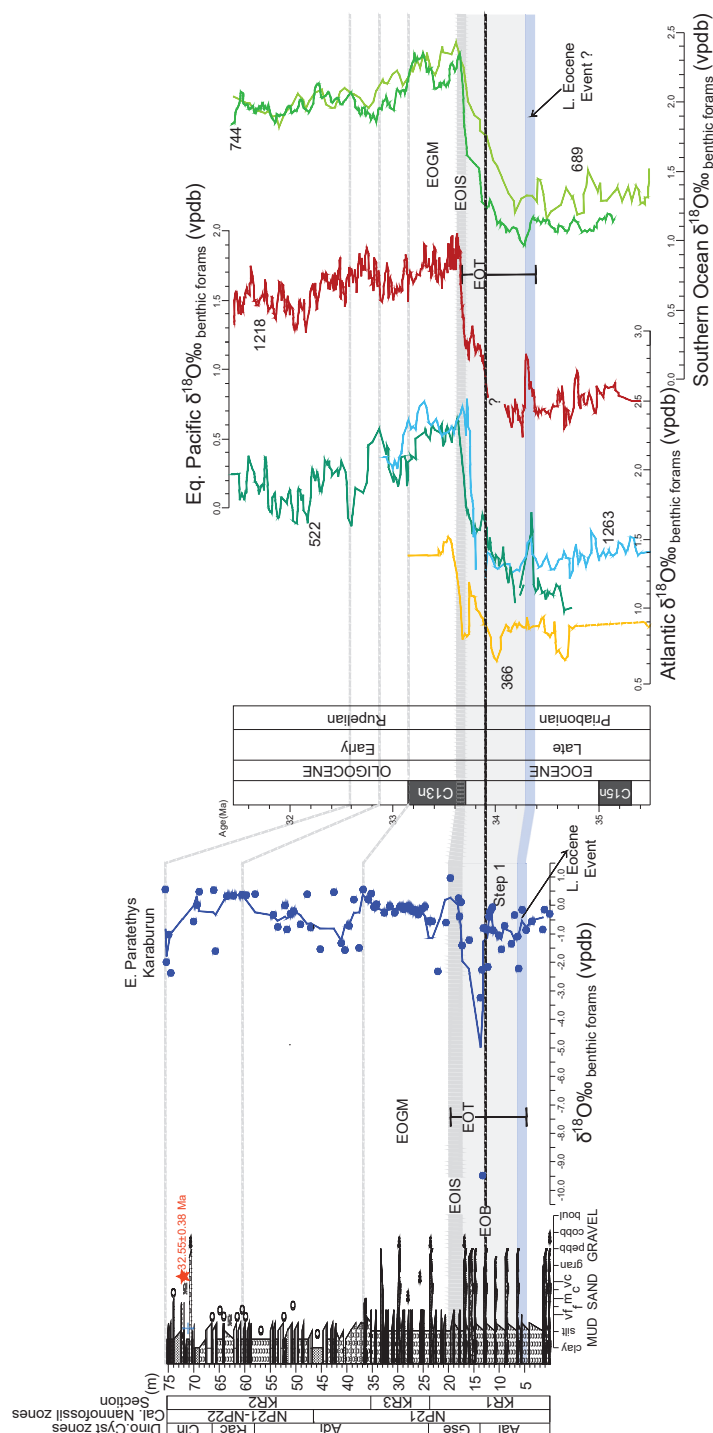


Figure 4 The stratigraphic log (in meters) of the Karaburun composite section including the results of benthic foraminifera $\delta^{18}\text{O}$ record (blue dots and line showing three-point running mean), highlighting the chronostratigraphic characteristics of the Eocene-Oligocene Transition (EOT). Apparent correlations were established by aligning the Karaburun data with high-resolution deep sea benthic foraminifera $\delta^{18}\text{O}$ records from the South Atlantic sites 522 (Zachos et al., 1996) and 1263 (Langton et al., 2016), and compared to the tropical Atlantic site 366 (Langton et al., 2016), the Southern Ocean sites 744 and 689 (Zachos et al., 1996; Diester-Haass and Zahn, 1996), and the equatorial Pacific site 1218 (Coxall and Wilson, 2011). Key features in the $\delta^{18}\text{O}$ records, such as positive and negative shifts and their amplitudes, were used to define EOT characteristics, including the Late Eocene Event, the Earliest Oligocene Oxygen Isotope Step (EOIS) and the Early Oligocene Glacial Maximum (EOGM). The Eocene-Oligocene Boundary (EOB) was identified through biostratigraphic analyses (see section 5.1). The red star on the log marks the tuff layer, while the blue cross indicates the occurrence of the cold-water dinocyst *Svalbardella cooksoniae*.

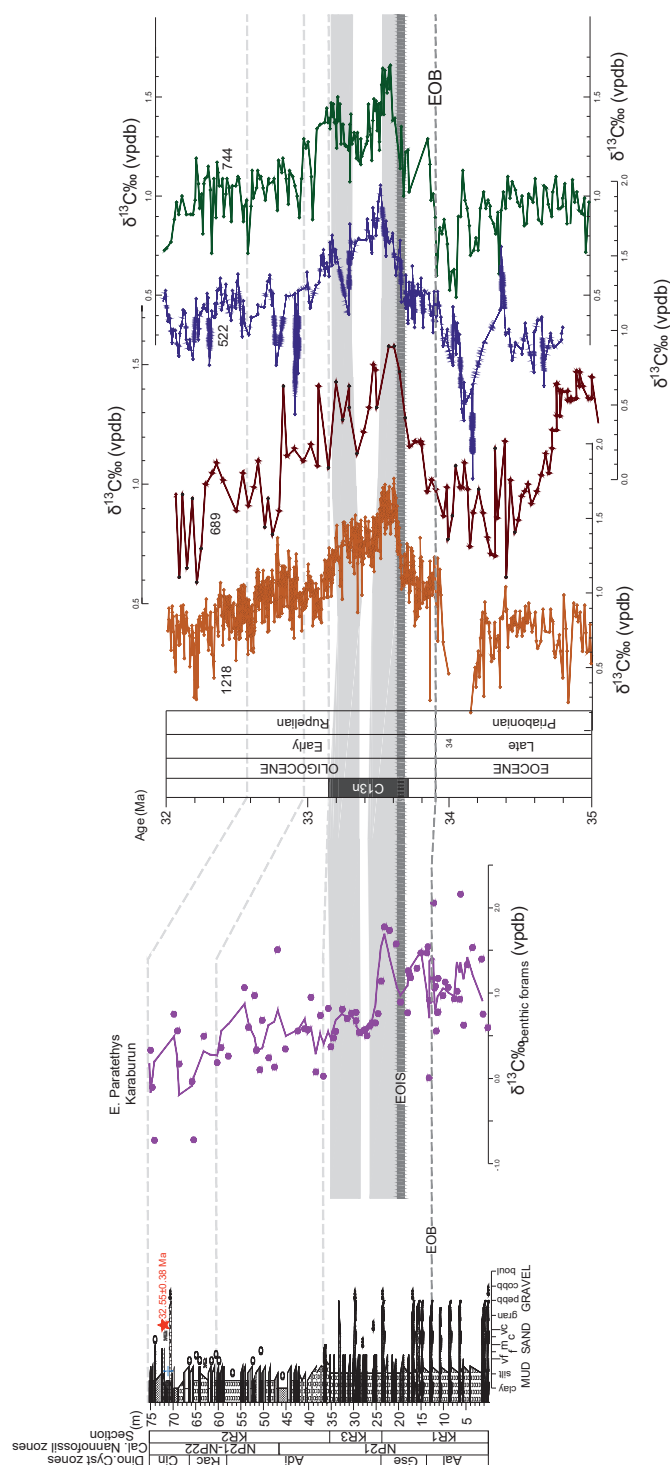


Figure 5 Benthic foraminifera $\delta^{13}\text{C}$ record (pink dots and line showing three-point running mean) of the Karaburun composite section along the stratigraphic log (in meters) highlighting the chronostratigraphic features of the Eocene-Oligocene Transition (EOT). Correlations were made with deep marine records from Site 689 in the sub-Antarctic Atlantic (Diester-Haass and Zahn, 1996), Site 1218 in the equatorial Pacific (Coxall and Wilson, 2011), Site 522 in the South Atlantic (Zachos et al., 1996), and Site 744 in the Southern Ocean (Zachos et al., 1996). Alignment of high-resolution benthic foraminifera $\delta^{13}\text{C}$ records from these sites with the Karaburun data revealed corresponding double peak isotope feature (gray shading) after the Earliest Oligocene Oxygen Isotope Step (EOIS) within the Early Oligocene Glacial Maximum (EOGM). The Eocene-Oligocene Boundary (EOB) was determined through biostratigraphic analysis (see section 5.1). The red star marks the tuff layer, while the blue cross indicates the level of sample containing the cold-water dinocyst *Svalbardella cooksoniae*.

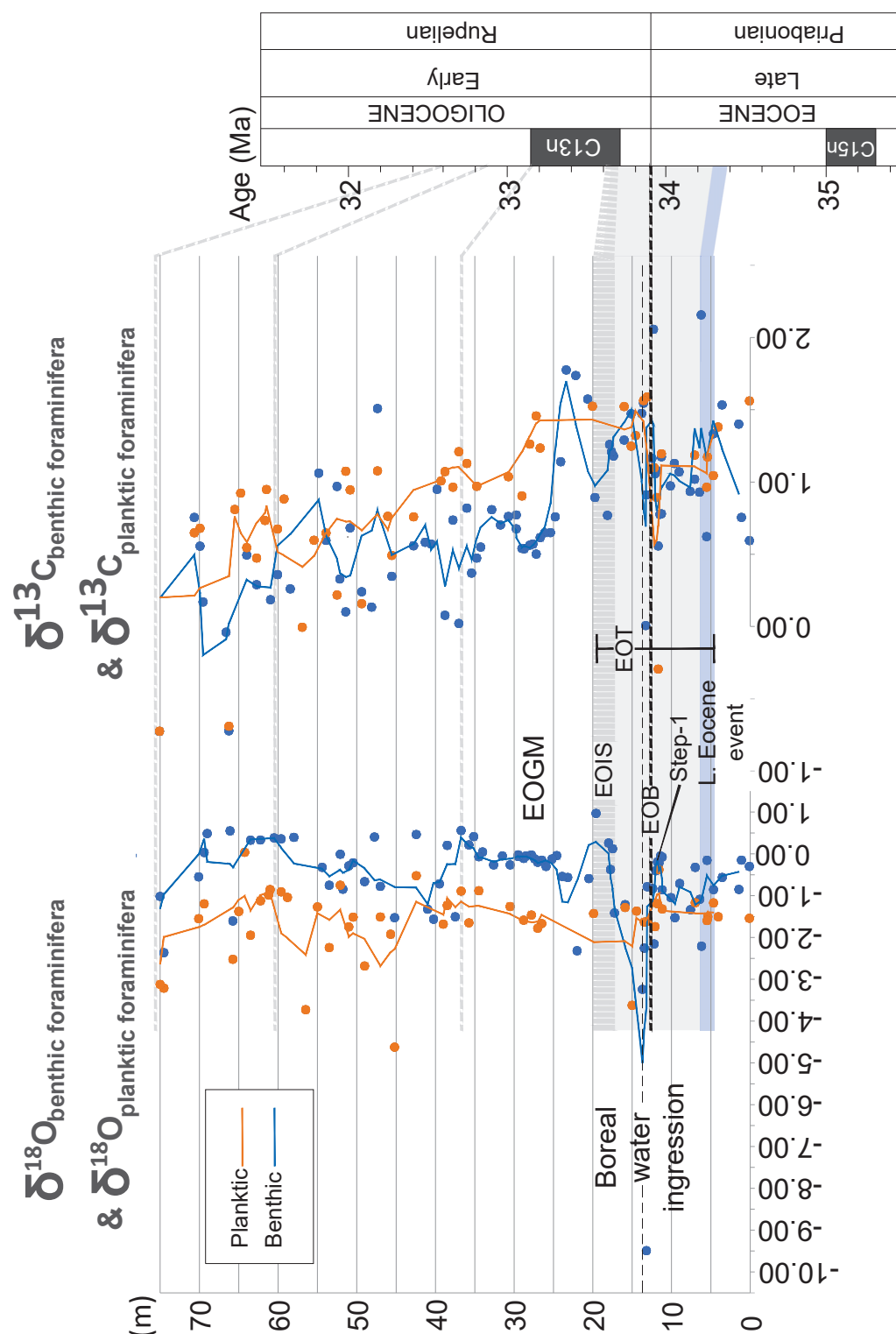


Figure 6 Oxygen ($\delta^{18}\text{O}$) and Carbon ($\delta^{13}\text{C}$) stable isotope values for the benthic and planktic foraminifera from the Karaburun composite section. The black dashed line represents the level for the boreal water ingress just after the Eocene-Oligocene Boundary (EOB). EOT: Eocene-Oligocene Transition. EOIS: Earliest Oligocene Oxygen Isotope Step. EOGM: Early Oligocene Glacial Maximum.

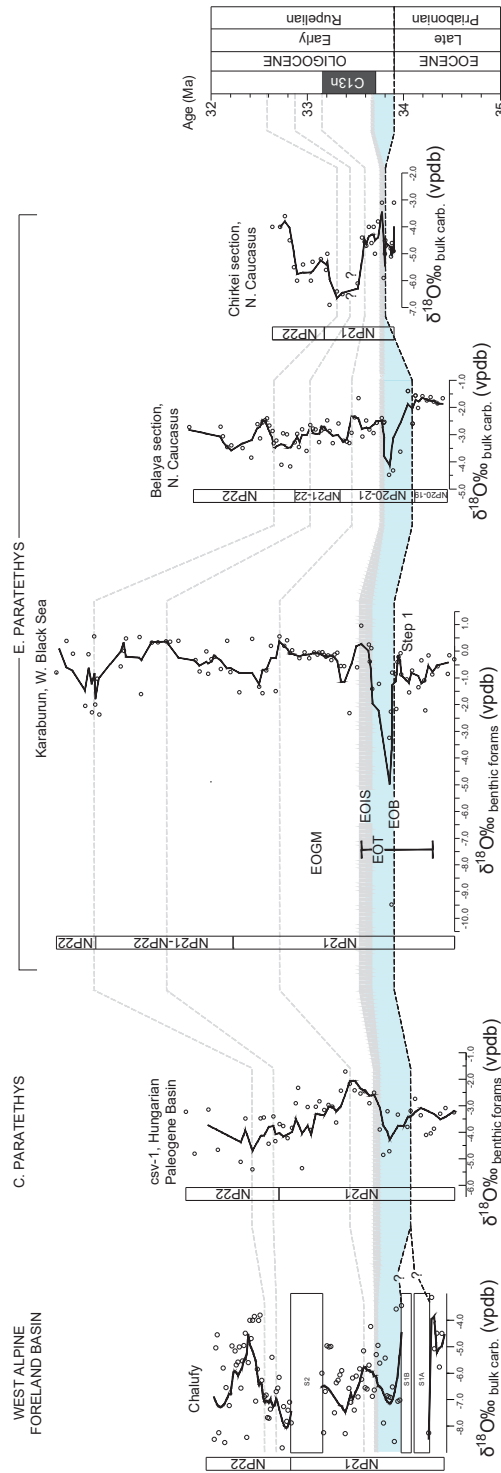


Figure 7 Oxygen stable isotope ($\delta^{18}\text{O}$) values and the characteristic negative $\delta^{18}\text{O}$ shift during the EOT observed in various Paratethys marine records. Correlations highlight the interval (light blue shading) between the Eocene-Oligocene Boundary (EOB) and the Earliest Oligocene Oxygen Isotope Step (EOIS, gray dashed line) across various sections, including the Chalufy Section in the West Alpine Foreland Basin, which links the Western Paratethys to the Mediterranean Tethys (Soutter et al., 2022); the csv-1 core from the Hungarian Paleogene Basin (Ozsvárt et al., 2016); the Karaburun Section (this study); and the Belaya (van der Boon et al., 2019) and Chirkei (Gavrilov et al., 2017) sections from the Northern Caucasus. To account for varying sample resolutions, a three-point running mean filter was applied uniformly to all sites.

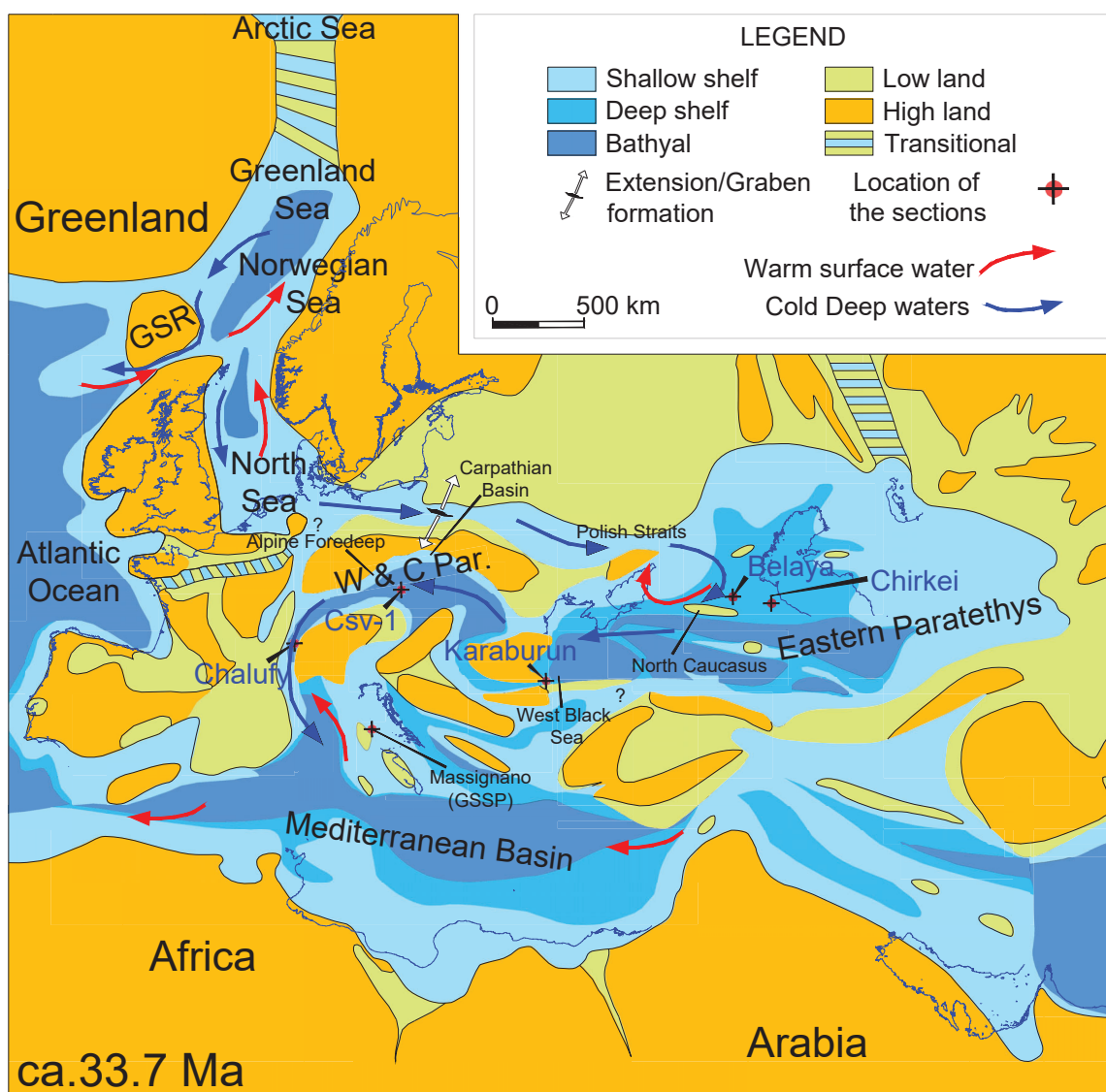


Figure 8 Paleogeographic map at 33.7 Ma (modified from Sachsenhofer et al., 2018) illustrating boreal water circulation through the Paratethys, extending into the Mediterranean Tethys. GSR: Greenland Scotland Ridge.